A new System Design Tool for a Hybrid Rocket Engine Application

Elena Quero Granado, Giulio Pelenghi, Jouke Hijlkema, Jérôme Anthoine, Jean-Yves Lestrade

A new System Design Tool for a Hybrid Rocket Engine Application

Elena Quero Granado⋆†, Giulio Pelenghi⋆, Jouke Hijlkema⋆, Jean-Yves Lestrade⋆ and Jérôme Anthoine⋆

⋆ *ONERA / DMPE, Université de Toulouse, F-31055 Toulouse, France*

elena.quero_granado@onera.fr · giuliopelenghi@gmail.com · jouke.hijlkema@onera.fr · jean-yves.lestrade@onera.fr · jerome.anthoine@onera.fr

† Corresponding author

Abstract

A system design tool allowing to simulate the complete operation of a hybrid rocket engine is developed in this paper. The algorithm of the application is made in such a way that allows the simulation of an element, an ensemble of elements or all the elements constituting a hybrid space propulsion system. The objective is to simulate and predict the behavior of the engine at different conditions / configurations during the first pre-design phases. As the tool will be exclusively used during these phases, a balance between the duration of the simulation and its precision must be reached. Given these constraints, a maximum error of 30% between the experimental and the numerical results is considered adequate to validate the solution. The main parts of our HYCAT engine -characterized by a catalytic injection of oxidizer- are modeled and included in this tool: the mass flow rate regulator and the catalyst (feed and injection sub-systems) through 0-D models; the combustion chamber with a 1.5-D model; and the nozzle through a 1-D model. An iterative method is employed to attain the pressure convergence in the combustion chamber between these three main parts of the engine whose corresponding system of equations is solved by a Newton-Raphson technique. Seven experiments performed on HYCAT are used to validate the results of the conceived tool. From all the performed simulations, only two of them present relative differences with the experiment above the defined threshold. The largest errors are produced for the fuel regression rate, the consumed mass of fuel, and the mixing ratio variables. The best agreements with the experiments are found for the simulations with the largest oxidizer mass fluxes (G_{ox} >230 kg/m^2/s) and where the mixing ratio is closer to the stoichiometric value, defining thus, the range of applicability of the system design tool.

Keywords: System design tool, hybrid rocket engine, 1.5-D combustion chamber model

Nomenclature

Letters

A	Cross-section area, m^2
A_d	Arrhenius preexponential constant, m/s
C_d	Discharge coefficient
c^*	Characteristic velocity in the nozzle, m/s
c_F	Thrust coefficient
c_p	Specific heat coefficient, J/kg/K
$\mathcal{D}$	Diffusion coefficient, m^2/s
D	Diameter, m
E_a	Activation energy in the Arrhenius pyrolysis law, J/mol
F	Thrust force generated by the propulsion system, N
G	Mass flux, kg/m^2/s
g	Gravity, m/s^2
H	Height, m
h_D	Mass diffusion coefficient, m/s
h_t	Specific total enthalpy, J/kg
h_{conv}	Heat convection coefficient, W/m^2/K
I_{sp}	Specific impulse of the engine, s
L	Length, m
Le	Lewis number
$\mathcal{M}$	Molar mass, kg/mol
M	Mach number
m	Mass, kg
$\dot{m}$	Mass flow rate, kg/s
N	Number of points of the mesh along the axis
N_{sp}	Total number of species in the gas flow
P	Pressure, Pa
Pr	Prandtl number
$\dot{Q}$	Heat flux, W/m^2.
R	Radius, m
$\mathcal{R}^2$	Coefficient of determination
R_g	Gas constant, J/kg/mol
r	Radial coordinate (reference from the axis), m
S	Surface, m^2
T	Temperature, K

t	Time, s
u	Axial velocity component, m/s
V	Volume, m^3
v	Radial velocity component, m/s
v_r	Fuel regression rate, m/s
x	Axial coordinate
Y_k	Mass fraction of species k
y	Radial coordinate (reference from the fuel surface), m
α	Angle measured with respect to the symmetry axis, degrees
γ	Heat capacity ratio
Δ	Difference between the values of a variable in the current and the previous stage / position
Δh_{pyr}	Specific enthalpy of pyrolysis of the fuel, J/kg
Δv	Impulse per unit of spacecraft mass needed to perform a maneuver, m/s
ϵ	Void fraction of the catalyst bed
ε	Relative difference of a variable with respect to a reference value, %
η	Efficiency of the system / process
λ	Thermal conductivity, W/m/K
μ	Dynamic viscosity, Pa·s
ρ	Density, kg/m^3
Σ	Expansion ratio of the nozzle
ϕ	Mixing ratio
$\dot{\omega}_k$	Production rate of species k at the fuel surface, $kg/m^2/s$

Subindex

ad	Corresponding to the adiabatic conditions
amb	Evaluated at ambient conditions
c	Corresponding to combustion
cat	Referring to the flow in the catalyst / catalytic injection
cat, p	Referring to the catalyst particles
ch	Referring to the combustion chamber (fuel block)
$cond$	Corresponding to the conduction phenomena
con	Referring to the convergent part of the nozzle
$conv$	Corresponding to convection
$diaph$	Referring to the diaphragm of the engine injection sub-system
$diff$	Corresponding to diffusion
div	Referring to the divergent part of the nozzle
e	Referring to the core flow in the combustion chamber
exp	Corresponding to the experiment
f	Corresponding to the solid fuel
$final$	Corresponding to the state at the end of the burn
fl	Corresponding to the flame in the combustion chamber
hyb	Corresponding to the hybrid phase of the engine
$i = 1, 2, ..., N$	Referring to the position (node) in the axial mesh
$init$	Corresponding to the initial conditions
inj	Referring to the entrance to the catalytic injection
$nozzle$	Referring to the nozzle
num	Corresponding to the numerical simulation
out	Conditions at the exit of the engine
ox	Referring to the oxidizer
pyr	Corresponding to fuel pyrolysis
ref	Reference value
reg	Corresponding to the mass flow regulator / valve element of the engine
s	Referring to the fuel surface
st	Corresponding to the stoichiometric conditions
$tank$	Corresponding to the oxidizer tank
th	Corresponding to the nozzle throat
$trans$	Referring to the transient regime
$vessel$	Referring to the vessel used in the communicating vessel technique for the fuel grain diameter measurement
w	Corresponding to the water used in the communicating vessel technique for the fuel grain diameter measurement

Superindex

geo	Corresponding to the geometric measurement
vc	Corresponding to the conservation of volume

Acronyms/Abreviations

Boundary Layer: BL
Computational Fluid Dynamics: CFD
Chemical Equilibrium Applications: CEA
Central Processing Unit: CPU
European Space Agency: ESA
European Space Propulsion System Simulation: ESPSS
High-Density Poly-Ethylene: HDPE
Hybrid Rocket Engine: HRE
Newton-Raphson: NR
Oxidizer to Fuel ratio: O/F

1. Introduction

A Hybrid Rocket Engine (HRE) is a space propulsion system that relies on the chemical reaction of two propellants (the oxidizer and the fuel) stored at different states of the matter. The oxidizer, generally stored in the liquid or

gaseous phase in a tank, is injected -via a catalyst or a liquid or gaseous injector- into the combustion chamber, where the fuel is stored in the solid state. The high temperature of the injected gases generated by a pyrotechnic ignition device or a catalytic decomposition yields the pyrolysis and evaporation of the solid fuel, allowing the combustion process between both the fuel and the oxidizer. This process is governed by a self-sustained turbulent diffusion flame located in the boundary layer (BL) at a certain distance from the wall. Finally, the high temperature products are ejected and accelerated through the nozzle, generating, thus, the thrust of the engine. This technology is characterized by a high vacuum specific impulse ($\sim$ 360 s), superior to that of the solid propulsion, and presents a throttability capacity combined with a simple and safe operation of the engine for a low manufacturing cost. These features make it a very attractive technology, turning it into a feasible alternative to the more classical bi-liquid or solid space propulsion systems.

The development of numerics has boosted the conception of complex 2-D/3-D combustion chamber models of HREs. This fact has allowed the diminution of the number of necessary experimental campaigns and thus, the associated costs to characterize the behavior of an engine design at different conditions. In contrast, CFD models are able to determine quite accurately the local fuel regression rate along the wall when considering a more detailed chemistry, the flow turbulence and the radiation phenomena in the combustion chamber -accuracy of spatial and temporal averaged values above 15% [1, 2, 3]-, by also using less economic and material/human resources. Nevertheless, the computation time required to complete a steady-state simulation of the combustion chamber and retrieve the information of the variables that characterize this component can be very high for the first pre-design phases of the engine (several hours of CPU). Moreover, they mostly provide a solution of the combustion chamber and the nozzle components but not of the complete propulsion system and operation, thus not permitting to analyze the variables of the engine throughout the firing.

Several system design tools have been developed in order to study the behavior of a HRE over the whole duration of the test [4, 5, 6, 7]. These ones implement 0-D or 1-D models of the main parts constituting this kind of engine by using mass and energy balances. The elements generally modeled are:

- The feed sub-system with a pressure-regulated feed operation (pumps) or a self-pressurized tank (blowdown process), which determines the injected oxidizer mass flow rate.
- The combustion chamber, with a description of the fuel regression phenomenon through an empirical law that allows the calculation of the instantaneous consumed mass of fuel.
- The nozzle (characterized by a choked flow) that determines the pressure in the combustion chamber, and from there, the thrust and specific impulse of the engine.

These tools make use of iterative or sequential algorithms to solve the corresponding equations and retrieve the variation of the desired variables in time. The European Space Propulsion System Simulation (ESPSS) is a simulation platform developed for the ESA and composed of an ensemble of libraries containing models of the components of any space propulsion system (hybrid, solid or bi-liquid) [8]. It allows to solve individually any element or ensemble of elements -specified by the user-, as well as to add new models that can be integrated into the application. Furthermore, other tools with similar characteristics than the ones described above have been conceived, but which also make use of optimization algorithms [9, 10, 11] to obtain the set of parameters (spacecraft mass, Σ, combustion chamber pressure, ϕ, etc.) that provide the best engine design achieving the mission requirements (total spacecraft mass, Δv). Concerning the work in our laboratory, SOPHY tool was conceived for CNES to rapidly evaluate the operation of a HRE. This one also implemented an empirical model to characterize fuel pyrolysis and a sequential resolution algorithm using the values at the previous time step to obtain the variables at the current step.

Notwithstanding, the fitting coefficients of the empirical regression rate laws used in these applications depend on the Oxidizer / Fuel couple (O/F) employed and the test conditions, such as the type of injection, the size of the engine or the geometry of the fuel block, among others. Hence, they cannot be generally applied into a system design tool for the simulation of a HRE at any configuration, since, in order to obtain a good estimation of these coefficients, the experimental results of the regression rate at the conditions to be simulated should already be available. Therefore, in order to conceive a system design tool that can simulate any HRE, a combustion chamber model keeping a compromise between the computational cost of 0-D regression rate models and the precision of CFD simulations must be developed. This tool is meant to be applied during the pre-design phases of the engine. In this way, a maximal error of 30% is authorized to account for the differences between the real (experimental) values of any variable and the ones obtained by the simulation, especially, for the regression rate variable.

To this extent, an approximate 2-D combustion chamber model (also known as a 1.5-D model) has been developed. It is based on the integral BL methods and reproduces the most important physical phenomena inside the

chamber (BL development, heat and mass exchanges with the fuel surface). This kind of models has been used in literature before to simulate non-reactive and reactive flows [12, 13], proving to be less time-consuming in comparison to a full Navier-Stokes solver while supplying satisfactory results.

Therefore, a description of the HRE of our laboratory (HYCAT) and the seven experimental tests performed on this one are made in this paper. Then, the models of the main elements characterizing this engine (including the aforementioned pseudo-2-D combustion chamber model) are developed and implemented into a newly-conceived system design tool, which, as for the ESPSS software, allows the user to develop and easily integrate new models of other engine components into the tool, as well as to specify whether to simulate any element or ensemble of elements of the HRE. Eventually, the numerical results obtained with our tool are assessed and compared with the performed HYCAT tests, and the final conclusions concerning the applicability and validity of this code are drawn.

2. Materials and methods

In this section, the materials and methods employed for the development and validation of the new system design tool are presented.

2.1 HYCAT engine test bench

HYCAT (HYbrid with CATalyst) is the lab-scale HRE built in our laboratory that has been employed to perform the experimental tests used to validate the system design tool developed in this article. Engine ignition happens thanks to the injection at high temperature of the oxidizer mixture of hydrogen peroxide (H_2O_2) and water, which is chemically decomposed in a catalyst. Therefore, no use of a pyrotechnic device is made to ignite the engine. This means that the ignition does not happen immediately, and two stages are distinguished: the monopropellant phase, where the oxidizer is injected without any combustion reaction taking place; and then, the *hybrid* phase, where the fuel pyrolysis and the combustion processes begin, producing the rise of pressure and temperature in the combustion chamber. The test ends when the oxidizer valve is closed, entailing a sharp decrease in pressure until reaching the atmospheric value.

Figure 1 represents the schematics of the HYCAT engine, depicting its main components and highlighting the locations of the experimental measurements. Figure 2 is a picture of this HRE. HYCAT is constituted by the following main parts:

- **Oxidizer tank**. The liquid hydrogen peroxide is stored in a tank where the pressure is controlled and maintained at an approximately constant value throughout the test thanks to an external pressurization system with He gas. As a result, a roughly constant oxidizer mass flow rate is supplied to the propulsion system. Here, a strain gauge pressure sensor provides the pressure measurements. Indeed, as it will be analyzed more in depth in Sec. 4.1.1, these measurements display a high-frequency noise, but of an amplitude that remains below 0.1 MPa. From the tank, the oxidizer is driven into the propulsion system through an injection line.
- **Mass flow regulator / oxidizer valve**. The function of these elements is to control the flow of oxidizer that is injected from the tank into the combustion chamber. It is composed of a diaphragm that reduces the passage section of the flow, deviating its path and producing by consequence a pressure drop. Here, the section of the orifice and the pressure difference through this one will determine the mass flow rate, whose value is measured by a Coriolis flowmeter. Another strain gauge pressure sensor is employed to measure the pressure after the diaphragm section, previous to the entrance of the flow into the catalytic chamber.
- **Catalyst**. The catalytic injection of oxidizer produces the chemical decomposition of the liquid hydrogen peroxide and water mixture into a gaseous mixture of di-oxygen and water vapor [Eq.1] at high temperature (900-1200 K depending on the H_2O_2 concentration) that will ignite the engine. This kind of injection allows to improve the combustion efficiency with respect to an atomized injection due to the enhancement of the mixing with the pyrolyzed fuel gases and the avoidance of any energy losses required to heat and vaporize the liquid oxidizer [14]. This sub-system is composed of a liquid injection plate, a closed Inconel cylindrical chamber -of dimensions $D_{cat,ch} = 50$ mm and $L_{cat,ch} = 80$ mm- with a refractory steel mesh that stores and retains the $Al_2O_3 - Pt$ catalyst particles inside; and a gas injector that consists of an annular ring of the same diameter than the initial internal diameter of the fuel block. Several measurements of the catalytic decomposition temperature are provided by three type-K thermocouple sensors.

$$xH_2O_2 + (1-x)H_2O \rightarrow \frac{x}{2}O_2 + H_2O \tag{1}$$

- **Combustion chamber**. It is constituted by a stainless steel cylindrical shell that contains the fuel grain. The catalytic injection of the oxidizer at high temperature into the combustion chamber entails the pyrolysis of the solid fuel whose products react with the injected oxidizer gas. Two pressure measurements are performed at the entrance of the chamber. Furthermore, three ultrasonic sensors (US) distributed along the chamber provide measurements of the instantaneous fuel burnt thickness. In order to evaluate the instantaneous burnt thickness of the fuel block, the accurate temperature effect on the modification of the US wave propagation time needs to be quantified. However, since a reliable method to retrieve this effect has not been implemented yet, the measurements of these sensors will not be used in this paper to obtain the regression rate.
- **Post-combustion chamber**. This part of the engine is an extension of the combustion chamber where the mixing and combustion of propellants continues in order to improve the combustion efficiency. Here, two sensors allow to obtain the pressure measurements.
- **Nozzle**. A convergent-divergent carbon Laval nozzle is used in our HRE. The thrust forces are measured here by a three-component dynamometer.

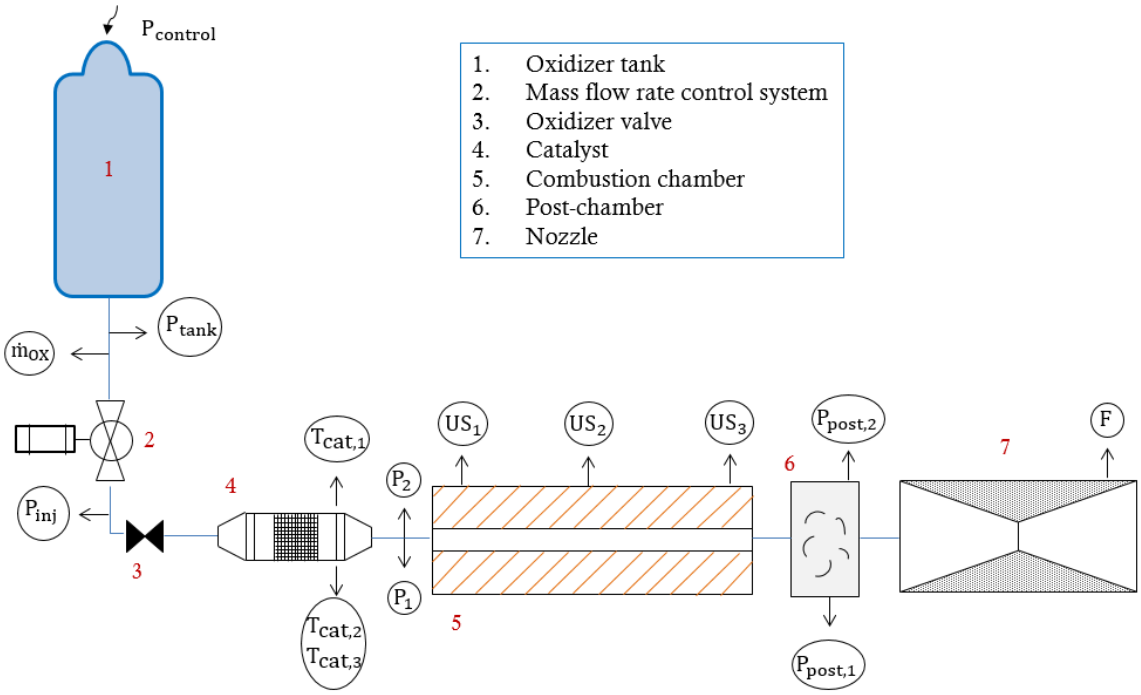

Figure 1: Schematics of the HYCAT engine.

In order to retrieve the evolution of the space-averaged regression rate with time, a ballistic reconstruction technique has been used. The implemented method is based on the one developed by Messineo et al. [15]. It assumes a constant value of the combustion efficiency ($\eta_{c,ch}$) while employing the experimental average pressure data in the combustion chamber and the oxidizer mass flow rate to determine the instantaneous regression rate.

In addition to the ballistic reconstruction method, the fuel block has been weighted at the start and at the end of the test, allowing to determine the total burnt mass of fuel after the test and thus, the final space-averaged diameter through volume conservation [see Eq. (2)]. An estimate of the space-time averaged regression rate can be computed from this final diameter using Eq. (3). This prediction can also be made by using the local final diameter measurement of the block at the end of the test and by averaging its value along the axis, resulting in $\bar{D}^{geo}_{ch,final}$. Throughout this paper, ($\bar{\cdot}$) will symolize the space-averaged value of a quantity.

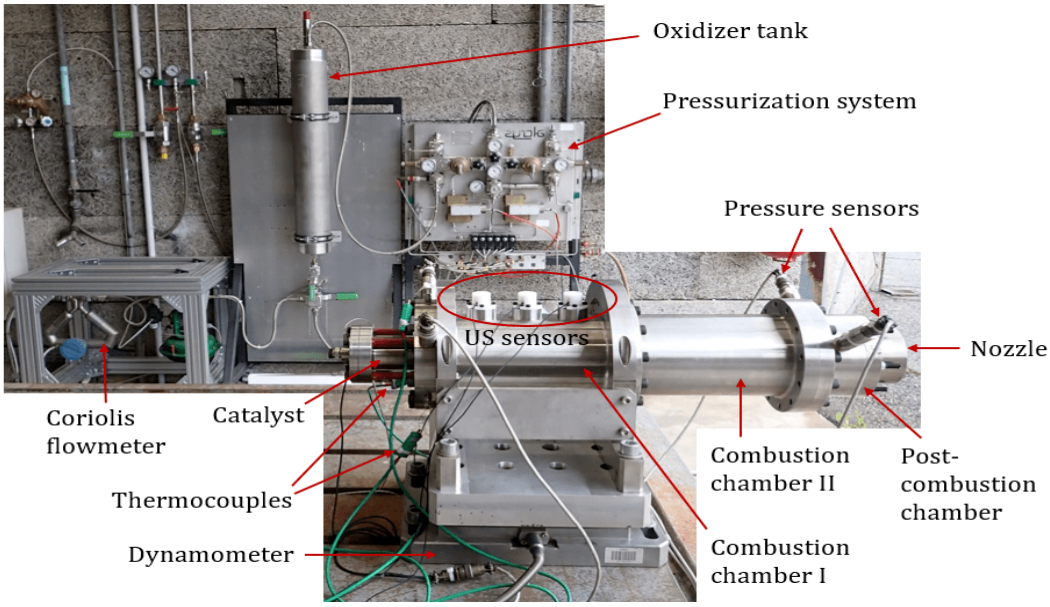

Figure 2: Main components and sensors of the HYCAT engine.

$$\bar{D}^{vc}_{ch,final} = \sqrt{D^2_{ch,init} + \frac{4\Delta m_f}{\pi \rho_f L_{ch}}} \tag{2}$$

$$\bar{v}_r = \frac{\bar{D}_{ch,final} - D_{ch,init}}{2t_{hyb}} \tag{3}$$

In HYCAT 12, 23 and 26 tests, this local diameter was obtained with a micrometer (assuming a circular cross-section channel) at eight different axial positions by cutting the fuel block in several slices. However, another method to determine the local diameter at the end of the burn and preserve at the same time the integrity of the block during and after the measurement was developed for tests 46, 47, 48 and 49. This method has been named *the communicating vessel approach* and its principle is presented in Sec. 2.2.

2.2 Geometric diameter measurement: the communicating vessel approach

The communicating vessel approach makes use of the hydrostatic concepts of fluid mechanics to retrieve the local diameter over the length of the fuel block. This measurement technique, developed in our laboratory, has already been briefly presented in Glaser et al.'s work [16]. The conceived set-up is composed of a hose that connects the fuel grain (whose local diameter is to be measured) with a transparent vessel of circular section equipped with a millimetric ruler. Both elements are placed in the vertical position, and the zero-mark of the transparent tube is located at the same height level as the base of the fuel grain (see Fig. 3).

The method consists in measuring the volume of water (V_w), introduced into the system by a syringe, that is required to produce a specific increase in the fluid level observed in the transparent tube (ΔH). By hydrostatics, because both elements (the fuel grain and the vessel) are open volumes to the environment (at ambient pressure), no pressure differences are present in the system, and the water level measured in the transparent tube is equivalent to the level of water that is present in the fuel grain. To start the measurement procedure of the grain diameter, the system is filled with water until the zero-mark of the vessel is attained. Then, the water filling process will be repeated until the fluid level reaches the top of the grain. Finally, the local diameter of the grain can be calculated by assuming a circular section. Thanks to the conservation of the fluid's volume in the system, Eq. (4) is obtained:

$$D^{geo}_{ch,final}(x) = \sqrt{\frac{4\Delta V_w}{\pi \Delta H} - D^2_{vessel}} \tag{4}$$

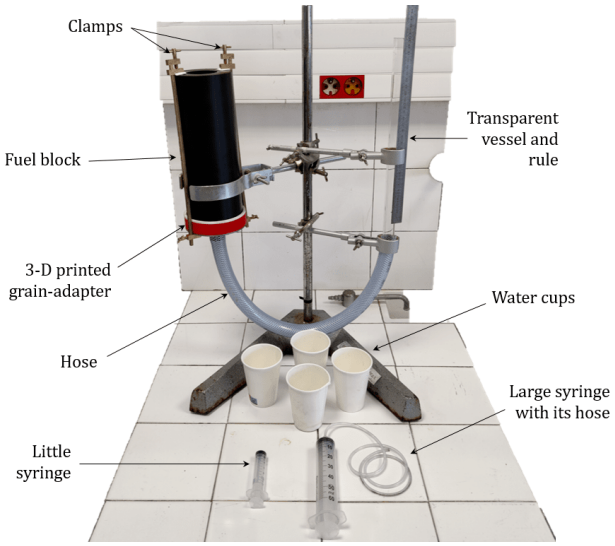

Figure 3: Communicating vessel set-up for the measurement of the fuel block's internal diameter.

During the measurements, it was verified that no water leaks were present in the multiple connections between the elements. This was thanks to the use of a 3-D printed adapter and several o-rings placed on the fuel grain base, which were kept together and linked to the system by a pair of clamps. Four repeated measurements performed on the same fuel block allowed us to assess the reproducibility of the experiment and quantify the uncertainties of the measurement technique. The produced errors would be associated to capillarity effects, parallax, syringe filling, etc.

2.3 HYCAT experimental tests

In order to proceed to the validation of the system design tool developed in this paper, a total of seven tests performed on the HYCAT engine using an axial injection of 87.5% H_2O_2 as oxidizer and HDPE as the solid fuel have been conducted: the HYCAT tests 12, 23, 26, 46, 47, 48 and 49. Table 1 gathers the information of the geometrical characteristics for all of them as well as the targeted mass flow rate of oxidizer and the duration of each test. The objectives behind the realization of these tests were: to analyze the effect of the oxidizer mass flux (G_{ox}); to assess the experimental influence of the fuel port size in comparison to the numerical result; and finally, to evaluate the experimental and numerical impact of $\phi = \dot{m}_{ox}/\dot{m}_f$ produced by modifying the length of the block for a given mass flow rate and a specific port size of the grain, which will generate a growth in fuel consumption due to the larger burnt surface. Fuel densities (computed as V_f/m_f) were found to be between 940 and 970 kg/m^3 for the tests performed. The specific firing results are presented in more detail in Sec. 4.

The experimental conditions and results of the HYCAT 12, 23 and 26 tests have been already published by Durand et al. [17]. From Table 1, we observe that tests 12 and 23 were realized at approximately the same oxidizer mass flow rate (around 100 g/s), with the main differences being the duration of the test and the combustion chamber pressure (nozzle throat diameter). On the contrary, HYCAT 26 test -of slightly longer duration than test 12- operated at a higher mass flow rate (about 200 g/s) and with a nozzle of the same dimensions as the one used in test 23. Tests 46, 47, 48 and 49 have been performed recently though, and their results have not been published yet. They have been realized at a higher targeted oxidizer mass flow rate (around 300 g/s). All of them were performed by burning the grain during a similar amount of time (around 10 s) and by using Laval nozzles of identical dimensions. The difference between them resided mainly on the dimensions of the fuel blocks. On one hand, HYCAT 46 and 48 grains have ports of the same size ($D_{ch,init}$ = 25 mm) whereas being of different lengths ($L_{ch} \approx 250$ mm and $L_{ch} \approx 500$ mm, respectively). On the other hand, the internal diameter of the blocks in tests 47 and 49 is larger than the ones from tests 46 and 48 ($D_{ch,init}$ = 40 mm), but the grains have the same length as tests 46 and 48, respectively. For the HYCAT 48 and 49 tests, a second stainless steel combustion chamber containing a fuel block of roughly the same dimensions as the one stored in the first chamber is mounted adjacent to the first one, practically doubling the length of the grain with respect to the other tests. This configuration corresponds to the one seen in Fig. 2.

Table 1: Configuration and conditions of the HYCAT 12, 23, 26, 46, 47, 48 and 49 tests.

Test	**HYCAT 12**	**HYCAT 23**	**HYCAT 26**	**HYCAT 46**	**HYCAT 47**	**HYCAT 48**	**HYCAT 49**
Targeted $\dot{m}_{ox}$, g/s	100	100	200	300	300	300	300
$D_{ch,init}$, mm	25	25	25	25	40	25	40
L_{ch}, mm	240	245	240	249	250	499	499
D_{th}, mm	7	12.4	12.4	16	16	16	16
Σ	6.3	6.3	6.3	4.3	4.3	4.3	4.3
t_{final}, s	8.2	20.2	10.0	10.1	10.1	10.1	10.2

Another important difference between the new tests performed (46, 47, 48 and 49) and the other ones (12, 23 and 26) resided in the distance between the former's lateral face of the fuel grains and the gas injector ring. Indeed, in the recent tests, the grains were located right next to the oxidizer injection, whereas a larger distance was left for the ensemble of tests 12, 23 and 26 -reason why the length of these grains is a bit shorter. By increasing the space between the grain and the injector, the effects of the flow, such as, the turbulence or the presence of a recirculation zone, will be more important, producing by consequence a larger regression of the lateral face where the flow is in contact with. The geometric conditions of the new grains were determined to avoid this problematic phenomenon during the post-processing of the tests.

3. Theory and calculation

In this section, the models of the main elements constituting the HYCAT engine are developed (Sec. 2.1). These ones are: the mass flow rate regulator, the catalyst, the combustion chamber and the nozzle. Then, the algorithm of the system design tool implementing all of them is presented.

3.1 0-D mass flow rate regulator model

The oxidizer mass flow injected into the combustion chamber ($\dot{m}_{ox}$) is influenced by the section of the diaphragm constituting the mass flow rate regulator and the pressure difference through the orifice. The flow coming from the tank and passing through this element is still completely in the liquid state, and thus, can be treated as incompressible. Therefore, the estimation of $\dot{m}_{ox}$ is made by employing the steady incompressible flow discharge coefficient equation [18] [Eq. (5)], where the variations of density and temperature are considered to be negligible and no heat losses through the walls are contemplated either.

Nevertheless, to obtain an accurate evaluation of the oxidizer mass flow rate, $C_{d,diaph}$, which accounts empirically for the viscous losses, must be well characterized. This coefficient has been determined from the experimental HYCAT tests in the range of $\dot{m}_{ox} \approx 100 - 300$ g/s. A parabolic law ($\mathcal{R}^2 = 1$) has been retrieved [see Fig.4], implying a decrease of $C_{d,diaph}$ with the increase of $\dot{m}_{ox}$, which is due to the more important viscous losses associated to the change in geometry (cross-section of the diaphragm).

$$\dot{m}_{ox} = A_{diaph} C_{d,diaph} \sqrt{2\rho(P_{tank} - P_{inj})} \tag{5}$$

Moreover, in order to simulate the transient phase in the combustion chamber and because Eq. (5) is formulated in the steady regime, a linear rise of $\dot{m}_{ox}$ from a zero value at the start of the operation of the engine until reaching its steady-state value -given by Eq. (5)- at $t_{trans,reg}$, is implemented. For the ensemble of the tests performed, it has been observed that the duration of this transient phase ($t_{trans,reg}$) is about 0.18 s.

3.2 0-D catalyst model

Several authors have developed complex 1-D and 2-D CFD reactive flow models of catalysts applied to space propulsion accounting for the two-phase flow inside and simulating the decomposition reaction kinetics through the Arrhenius law [19, 20, 21].

Nevertheless, in an attempt to ease the weight of the numerical computations, a simple 0-D model for the catalytic injection system has been implemented for the system design tool developed in this paper. In order to proceed to

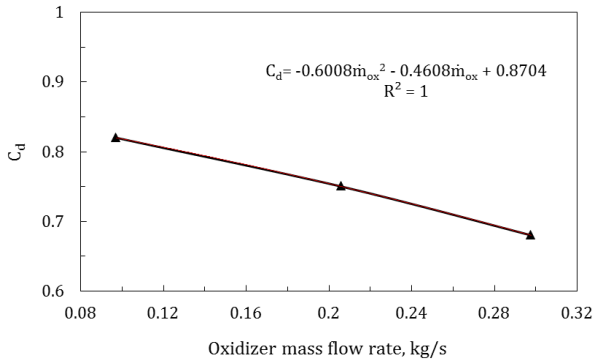

Figure 4: Effect of the oxidizer mass flow rate on the diaphragm discharge coefficient for the HYCAT tests.

the simulation of the combustion chamber, the variables such as the temperature (T_{cat}), the pressure ($P_{ch,0}$), and the oxidizer mass flow rate ($\dot{m}_{ox}$) at the exit of the catalytic injection (equivalent to the chamber entrance), are required. Through mass conservation, $\dot{m}_{ox}$ is considered to remain the same as the one computed in the mass flow rate regulator element [Eq. (5)]. The temperature at the exit of the catalyst is calculated by using Gordon and McBride's code [22] (CEA), which provides the adiabatic temperature of the chemical decomposition of H_2O_2-H_2O mixture for a specific initial temperature of reactants T_{inj} (system design tool input) and pressure $P_{ch,0}$ (unknown). Nonetheless, the actual (experimental) decomposition temperature is lower than the adiabatic value given by CEA. This effect is accounted by considering a decomposition efficiency ($\eta_{c,cat}$) between 0.94 and 0.98 [23].

The CEA decomposition temperature corresponds to the experimental value measured in the steady regime of the hybrid phase. Indeed, during the first part of the test (monopropellant phase), the temperature of the flow measured at the exit of the catalyst grows during the first 0.5 - 2.9 s from the value at which the oxidizer is injected into the catalyst ($T_{inj} \approx 290$ K) up to the steady decomposition value (CEA's value) in the hybrid phase. It is also noticed that the thermocouples installed at the exit ring of the catalytic chamber (green sensors in Fig. 5) provide temperature measurements (T_{cat}) that show a region where the temperature remains approximately constant at around 400 K -close to the water decomposition temperature value- just after the transient monopropellant phase and before the hybrid phase. However, for one of the sensors, the duration of this zone is much shorter. This discrepancy could be explained by the hysteresis phenomenon that these thermocouples can experience between 523 and 873 K (which can lead to several degrees of error), or could be due to the possible existing metallic contact with the gaseous injector.

Then, the temperature starts to increase faster until the injected temperature of oxidizer into the combustion chamber is high enough to vaporize the solid fuel and ignite the engine (hybrid phase), from where, T_{cat} tends to reach the decomposition value provided by CEA. Therefore, the duration of the transient phase described above can have a nonnegligible impact on the start of fuel pyrolysis. In order to remain in a simple modeling and simulate at the same time the aforementioned temporal variation of this variable, the corresponding evolution is approximated by a linear rise of the temperature from T_{inj} until the decomposition value defined by the product of $\eta_{c,cat}$ and CEA's adiabatic temperature ($T_{cat,ad}$) at $t_{trans,cat}$ [see Eq. (6)].


Figure 5: View of the catalytic chamber and the thermocouples mounted on the HYCAT engine.

Lestrade et al. [23] realized an experimental study of the catalyst employed in HYCAT, and found that pre-heating the catalyst, decreasing the size of the particles or increasing the oxidizer mass flow rate, contributed to reduce $t_{trans,cat}$. Therefore, an empirical expression to estimate the duration of the linear increase of the temperature leaving the catalyst and implemented in the model is developed in function of $\dot{m}_{ox}$, the surface of a single particle ($S_{cat,p}$) and the initial temperature of the catalyst ($T_{cat,init}$) [Eq. (7)]. The resulting formula is based on the experimental tests of Lestrade et al. [23] and Durand et al. [17], and has been built for a chamber of specific dimensions ($D_{cat,ch}$ = 50 mm and $L_{cat,ch}$ = 80 mm) filled completely with $Al_2O_3 - Pt$ catalyst particles. In Eq. (7), the empirical coefficients, computed by a fit nonlinear regression model, result in $B = 14.9588$, $m = -0.6867$, $p = 0.1792$ and $q = -0.1425$, and are characterized by an adjusted coefficient of determination of 0.898 and a root mean squared error of 0.0483. The use of this expression for another catalytic injection system using different particles, other storage conditions, or distinct dimensions of the catalytic chamber would require the adjustment of the aforementioned coefficients.

$$T_{cat} = \begin{cases} T_{inj} + \frac{\eta_{c,cat} T_{cat,ad}(Y_{H_2O}, P_{cat}, T_{inj}) - T_{inj}}{t_{trans,cat}} \text{ for } t < t_{trans,cat} \\ \eta_{c,cat} T_{c,ad}(Y_{H_2O}, P_{cat}, T_{inj}) \text{ for } t \geq t_{trans,cat} \end{cases} \tag{6}$$

$$t_{trans,cat} = B\, \dot{m}_{ox}^{m} S_{cat,p}^{p} T_{cat,init}^{q} \tag{7}$$

The energy of the system and therefore, the value of the adiabatic temperature computed by CEA are influenced by the pressure loss produced across the catalyst bed, which is related to the simultaneous kinetic (turbulence) and viscous energy losses. The Ergun equation for packed beds [24] has been applied to this extent. Equation (8) shows this formula expressed in International System (IS) units. Other authors have already used this same expression to estimate the pressure loss in reacting flows [19, 20], obtaining some satisfactory results in comparison with the experiments. This equation can be used for gaseous or liquid monophase flows, and depends on the unit depth of packed bed ($L_{cat,ch}$), the particle size ($D_{cat,p}$), the void fraction of the bed (ϵ), and some physical flow parameters such as the density and the average velocity ($\bar{u}_{cat}$) in the catalyst. The porosity ϵ has been obtained by using an empirical correlation [25] that uses the approximation of spherical catalyst particles [Eq. (9)]. The pressure at the entrance of the combustion chamber (exit of the gas injector ring) is considered to be the same as the pressure at the exit of the catalytic injection because hardly any pressure loss from one element to the other was retrieved experimentally.

$$\Delta P = \frac{L_{cat,ch}}{g} \frac{1-\epsilon}{\epsilon^3} \left(4826.1(1-\epsilon)\mu \frac{\bar{u}_{cat}}{D_{cat,p}^2} + 56.30 \frac{G_{ox} \bar{u}_{cat}}{D_{cat,p}} \right) \tag{8}$$

$$\epsilon = 0.375 + 0.34 \frac{D_{cat,p}}{D_{cat,ch}} \tag{9}$$

On account of the complexity of the physics involved, the transformation of the fluid from the liquid to the gaseous state is not modeled here, and the density and viscosity intervening in Eq. (8) are computed for the gas at the mean pressure and temperature between the inlet and exit parts of the catalytic chamber.

Equation (8) is formulated in the steady regime. Hence, the transient evolution of pressure in the monopropellant phase will not be correctly simulated. Indeed, at the beginning of this phase, Ergun's equation provides very large ΔP values associated with a rapid increase in the oxidizer mass flow rate, producing, as a consequence, negative numerical pressure values at the exit of the catalyst. In order to maintain the pressure lossses within physical limits during this phase, the instantaneous change in the flow velocity ($d\bar{u}_{cat}/dt$) is limited up to a specific value that has been found to be between 6 and 30 m/s^2 for the ensemble of the tests performed.

3.3 1.5-D combustion chamber model

A 1.5-D model is used to describe the physics in the combustion chamber of the HRE. This one is an approximate 2-D model based on the integral BL equations that involves the integration of the Navier-Stokes equations in the radial direction of the flow and the numerical simulation of the resulting equations along the axis of the channel. The main hypothesis behind the aforementioned model are the following:

- In the developing flow configuration, the flow is divided into a non-viscous zone (core flow) and a viscous region (BL).

- $Pr \approx 1$ and $Le \approx 1$, meaning that $\mathcal{D}$ is the same for all the species in the flow.
- The turbulent diffusion flame in the BL is described by an infinitely fast chemistry and a stoichiometric chemical equilibrium combustion, where the thermodynamic properties are obtained by Gordon and McBride's code [22] in a constant temperature-pressure problem. This combustion is described by a single global reaction: $F + n_{ox}Ox \rightarrow n_{CO_2}CO_2 + n_{H_2O}H_2O$, where only CO_2 and H_2O species are considered as the main products.
- Empirical radial distributions of the main variables (velocity, temperature and species mass fractions) are used to describe the flow in the BL by the application of the Reynolds analogy.
- The viscous stress term at the fuel surface is represented by a skin friction coefficient that is modified to take into account the blowing effect of the pyrolyzed fuel.

The description of the solid fuel pyrolysis (definition of the boundary conditions) is made through the Gas-Surface Interaction (GSI) model, which realizes the physical coupling between the fuel mass flow, the thermochemical conditions of fuel degradation and the reactive flow. It is based on the application of a global and species mass conservation balances [Eq. (10) and (11), respectively] and an energy balance [Eq. (12)] at the fuel surface. In this formulation, the radiative heat fluxes have been neglected, and only one species generated from fuel pyrolysis is considered (the most predominant one).

Additionally, the decomposition of fuel by ablation is expressed by an Arrhenius law [Eq. (13)]. These characteristics make the developed combustion chamber model reusable for other HRE configurations independently of the test conditions, since the estimation of fuel consumption depends on physical parameters (not empirical), and is, therefore, subject to the aerothermomechanical conditions of the flow.

$$\rho v \rfloor_s = \rho_f v_r \tag{10}$$

$$\rho v Y_k \rfloor_s - \underbrace{\rho \mathcal{D} \frac{\partial Y_k}{\partial y}\bigg|_s}_{h_D(T_{fl}-T_s)} = \dot{\omega}_k(T_s) \tag{11}$$

$$\underbrace{-\lambda_g \frac{\partial T}{\partial y}\bigg|_s}_{h_{conv}(T_{fl}-T_s)} = \underbrace{\rho_f v_r c_{p,f}(T_s - T_{ref})}_{\dot{Q}_{cond}} + \rho_f v_r \Delta h_{pyr} \tag{12}$$

$$v_r = A_d \exp\left(-\frac{E_a}{R_g T_s}\right) \tag{13}$$

Concerning the numerical simulation, the combustion chamber is discretized in N points or nodes along the axial direction (x_i, with $i = 1, 2..., N$), separated by a finite and constant distance (Δx). A finite difference method is used to discretize the equations of this 1.5-D model at each axial position. An unconditionally stable two-level implicit method is used for the time derivatives: the backward Euler first-order scheme, which evaluates the source terms at the current time step: $\Phi^{n+1} = \Phi^n + f\left(t_{n+1}, \Phi^{n+1}\right)\Delta t$. This makes it possible to take longer time steps without the risk of appearance of instabilities and thus, to reduce the number of iterations. Regarding the spatial scheme, a first-order backward difference scheme that uses the information of the previous spatial points to calculate the solution at the current position is employed. Spatial derivatives are thus calculated as $\frac{\partial \Phi}{\partial x} = \frac{\Phi_i - \Phi_{i-1}}{x_i - x_{i-1}}$.

Eventually, the set of equations at each point of the chamber is solved with a globally convergent Newton-Raphson (NR) algorithm (residual of 10^{-8}). This method combines the quadratic convergence of the classical NR method for the zero-root finding technique of a system of equations with the backtracking line search strategy, guaranteeing thus, the progress towards the final solution at each iteration. Once the solution at a specific position is found, the values of the variables at this point serve to compute the spatial derivatives in the equations of the next axial position, whose resolution is performed through the NR method. This procedure is afterwards applied to the rest of the combustion chamber points.

More details concerning the development of the integral flow equations and the first experimental validation of this 1.5-D combustion chamber model can be found in Quero Granado et al.'s previous work [26].

3.4 1-D nozzle model

The simulation of the flow inside the nozzle is of great importance since it defines the pressure in the combustion chamber, influencing thus the HRE performance. A 1-D nozzle model is developed at this extent for the system design tool by using the transient Euler (non-viscous) equations of continuity, momentum and energy for a compressible and isentropic flow. In this model, the properties of the flow are considered to be uniform across a section and vary only in the axial direction. In Appendix A, the governing equations of this nozzle model are presented in terms of the non-dimensional variables of velocity, pressure and temperature among others. In a first simplification, the Laval nozzle used in the HYCAT engine is approximated by a conic geometry in the simulation.

The same numerical algorithm of NR employed to solve the equations of the 1.5-D combustion chamber model (Sec. 3.3) is used to solve the 1-D equations described in Appendix A (implicit time scheme and first-order upwind spatial scheme).

Therefore, the variables of pressure, velocity, temperature and density at the entrance of the nozzle are needed to proceed to the resolution of the 1-D equations of this element. Their values are considered to be equivalent to the ones defining the state of the flow in the post-combustion chamber, where both the pressure ($P_{ch,N+1}$) and the velocity ($u_{e,N+1}$) are computed by applying the mass and momentum balances to the control volume delimited by the end of the combustion chamber and the entrance to the nozzle (post-combustion chamber). The temperature is computed by the CEA code for $P_{ch,N+1}$ and $\phi = \dot{m}_{ox}\Delta t / \sum_{i=1}^{N_{ch}} \Delta m_{f,i}$ by considering that the mixing of gases and the combustion are completed in the post-chamber. Finally, the ideal gas equation is applied to calculate the density.

In the simulation of the flow throughout the nozzle, it has been imposed that in the case of M_{th} being between 0.8 and 1 (transonic regime), a combination, in terms of pressure, between the subsonic and the supersonic solutions in the divergent part of the nozzle is performed by the definition of the parameter $\kappa = (1 - M_{th})/(1 - 0.8)$, which determines, in function of M_{th}, a proportional value of pressure between the subsonic and supersonic flow solutions in the nozzle. This allows to avoid any numerical instabilities or oscillations between the subsonic and supersonic solutions when searching for the converged result during the iterative process, as well as to simulate a soft transition from the subsonic to the supersonic flow. The subsonic and transonic solutions have been obtained during the monopropellant phase only, being the flow entirely supersonic in the hybrid phase.

The pressure needed in the combustion chamber to attain either a subsonic or a supersonic flow in the nozzle is given by the subsonic compressible flow [Eq. (14)] and the choked compressible flow equations [Eq. (15)], respectively.

$$\dot{m}_{out} = A_{out} P_{ch,N+1} \times \sqrt{\frac{2\gamma_{out}\mathcal{M}_{ch,N+1}}{R_g T_{ch,N}(\gamma_{out}-1)}\left[\left(\frac{P_{out}}{P_{ch,N+1}}\right)^{\frac{2}{\gamma_{out}}} - \left(\frac{P_{out}}{P_{ch,N+1}}\right)^{\frac{\gamma_{out}+1}{\gamma_{out}}}\right]} \tag{14}$$

$$\dot{m}_{out} = \frac{P_{ch,N+1} A_{th}}{\eta_{c,ch} c^*} \tag{15}$$

The thermodynamic properties of the flow (γ) throughout this element of the engine are obtained by the resolution of the theoretical rocket performance problem in the CEA code for an infinite area combustion chamber by using the pressure and the mixing ratio retrieved in the post-combustion chamber. Finally, the thrust of the engine and the specific impulse can be calculated by Eqs. (16) and (17), respectively.

$$\begin{cases} F = c_F P_{ch,N+1} A_{th} \\ c_F = \sqrt{\left(\frac{2\gamma_{out}^2}{\gamma_{out}-1}\left(\frac{2}{\gamma_{out}+1}\right)^{\frac{\gamma_{out}+1}{\gamma_{out}-1}}\left[1-\left(\frac{P_{out}}{P_{ch,N+1}}\right)^{\frac{\gamma_{out}-1}{\gamma_{out}}}\right]\right)} \\ \qquad + \frac{P_{out}-P_{amb}}{P_{ch,N+1}}\frac{A_{out}}{A_{th}} \end{cases} \tag{16}$$

$$I_{sp} = \frac{F}{\dot{m}_{out} g} \tag{17}$$

3.5 System design tool algorithm

The models of the elements presented in Sec. 3 are integrated into the system design tool. The algorithm of this tool is made in such a way that it allows the easy implementation of the developed models or any new ones as well as the simulation of the whole HRE or any element or ensemble of elements of the engine in fast computation times from a desktop computer.

In order to achieve the last requirement, an iterative convergence method between the three main sub-systems composing the HRE is employed. These ones are: the elements preceding the combustion chamber (feeding and injection sub-systems), the combustion chamber, and the nozzle. The application of the NR technique to solve simultaneously the system of equations of all the three sub-systems has been proven to be very time-consuming and more difficult to converge due to the great number of equations describing the combustion chamber (*number of variables* $\times N_{ch}$).

Because of HYCAT's pressurization system, the oxidizer tank pressure (P_{tank}) is an input of our system design tool. This parameter can be set to a constant value, follow a specified law over time, or be read from a *txt* file. In this way, once the input data for the tool have been introduced and the flow in the combustion chamber and the nozzle has been initialized, an estimation of the pressure at the entrance of the combustion chamber ($P_{ch,0}$) is imposed at the beginning of each time step of the simulation. This quantity is used to close and solve the system of equations characterizing the elements situated before the combustion chamber (the mass flow rate regulator and the catalyst), allowing the computation of the oxidizer mass flow rate, the pressure at the entrance of the catalyst and the decomposition temperature at the exit. With the knowledge of the mass flow rate, the temperature and the pressure at the entrance of the combustion chamber, this component of the engine can be completely simulated by using the sequential scheme (upwind spatial scheme) described in Sec. 3.3, solving the current node with the data from the previous one. This will then allow the calculation of the flow conditions in the post-chamber ($P_{ch,N+1}$) which should be equivalent to the conditions at the entrance of the nozzle.

Subsequently, the nozzle equations are solved, providing the pressure $P_{tuy,0}$ necessary at the entrance to develop a supersonic or subsonic flow in this element. In case that the absolute difference between the pressure obtained in the post-chamber from the resolution of the combustion chamber equations ($P_{ch,N+1}$) and the pressure at the entrance of the nozzle imposed by the flow through this one ($P_{tuy,0}$) is above a defined tolerance (10^{-5}), the pressure at the combustion chamber entrance, $P_{ch,0}$ is updated as $P'_{ch,0} = (P_{ch,0} - P_{ch,N+1}) + P_{tuy,0}$, which will be the new estimation introduced into the set of equations of the elements preceding the combustion chamber. The solution of the feeding and injection sub-systems will provide a new oxidizer temperature and mass flow rate injected into the combustion chamber, which will generate different $P_{ch,N+1}$ and $P_{tuy,0}$ values, whose equivalence will be verified again.

This process will be repeated until attaining the convergence criteria specified for the pressure in the combustion chamber. Once the condition is satisfied, the fuel block geometry is updated through the computed regression rate at each point along the axis of the channel, and the new geometry is used at the next time step. The simulation ends at the time indicated in the input data file of the system design tool or when all the fuel at any position of the grain has been consumed. Eventually, all the computed variables over time and along the axis of the engine (for the 1-D models) are stored in a *txt* file. Figure 6 depicts the workflow diagram representing the functioning of the conceived system design tool.

Concerning the numerical resources demanded by the system design tool to compute a HRE with the models presented in this article, it has been observed that the computation time is very dependent on the spatial discretization of the combustion chamber (Δx), but especially on the temporal discretization (Δt) chosen for the simulation of the full propulsive system. Indeed, the computing CPU time of the implemented numerical algorithm follows a power law of the form of $N_{ch}^{0.794}$ with the number of points constituting our lab-scale combustion chamber; and an expression showing the increase of the computing time (in minutes) with the time step (in seconds) of the form $\Delta t^{-0.829}$. In general, using the presented pseudo-2-D model for the simulation of a combustion chamber (constituted by an optimized and converged mesh of 100 nodes), together with a 1-D nozzle model of 800 points and the 0-D models described in Secs. 3.1 and 3.2, a converged solution at a specific instant of the test can be obtained in around 4 seconds of CPU time on a desktop computer. With regard to a complete HRE simulation of a firing of 10 s duration, by using an appropriate time step of 0.1 s, a result computed by the system design tool can be obtained in around ten minutes of CPU time on a desktop computer.

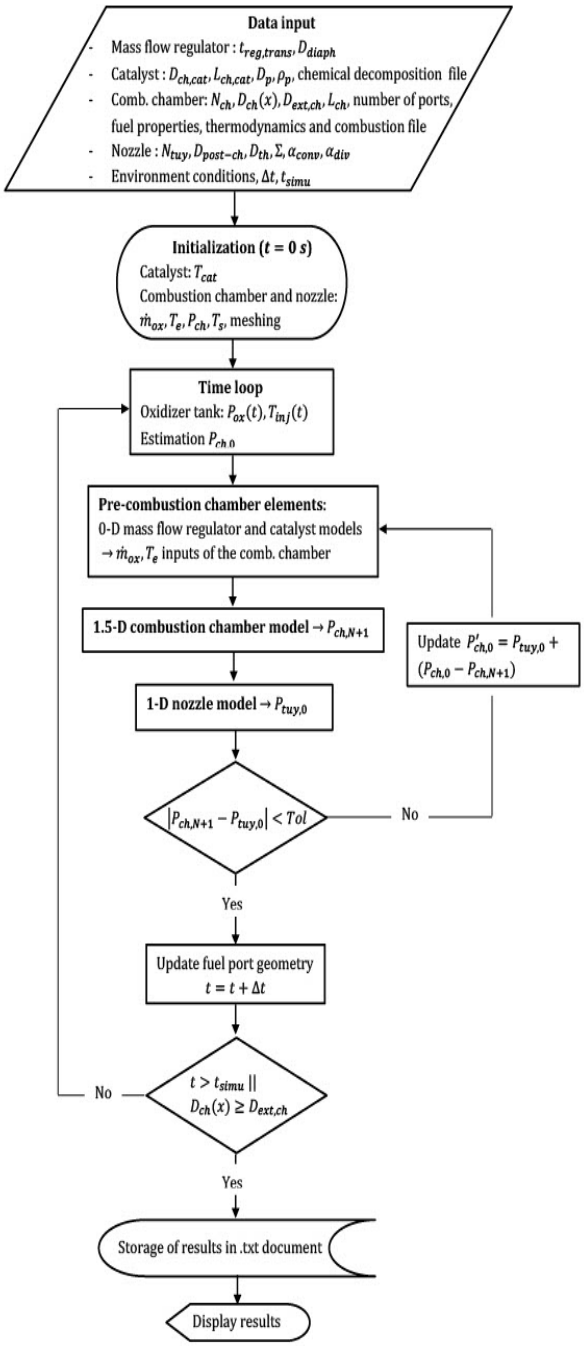

Figure 6: Flow chart diagram of the system design tool.

4. Resuts and discussion

In the present section, the experimental validation of our system design tool implementing the models presented in Sec. 3 is assessed. In particular, the HYCAT 48 test is analyzed in more detail (see Secs. 4.1.1 and 4.1.2). A summary of the experimental averaged measurements of the main variables in the hybrid phase and their relative differences with respect to the numerical results is presented afterwards (Sec. 4.2). Eventually, the validity region for the use of the HRE simulation tool will be determined.

Table 2: Thermophysical properties of HDPE [27, 28] employed in the computations.

A_d	E_a	ρ_f	$c_{p,f}$	λ_f	Δh_{pyr}	T_{vap}	T_{pyr}
4780	125.604×10^3	960	1850	0.4	2.72×10^6	415	720

For all the computations, the same thermophysical properties of the HDPE fuel -based on literature data- have been used. These ones are summarized in Table 2.

4.1 Comparison with the HYCAT 48 test

The interest of having chosen HYCAT 48 test to be studied in more detail in the upcoming subsections resides in the fact that this test has not been presented in previous studies yet. Moreover, the fuel port of the grain has the same size as the fuel blocks from the previous experimental tests already published (12, 23 and 26) [17], but with the main difference being the larger targeted oxidizer mass flow rate. Because the thrust could not be measured in test 46, test 48 was preferred to be analyzed in this section despite employing a longer grain than the previous tests. The input numerical conditions introduced into the system design tool in this case, are defined in Table 3. The input data for the rest of the tests have been updated to meet the conditions of the experiment to be simulated. Figure 7 captures an instant of the HYCAT 48 firing once the hybrid phase has reached the steady state. A longer and brighter flame is observed in comparison with the one from test 46 (with a shorter combustion chamber and similar input conditions). Indeed, as it will be seen later, the performances of test 48 are better than 46 (mixing ratio closer to the stoichiometric one and higher regression rates), which contributes to produce a more powerful flow ejected from the nozzle.

Table 3: Numerical inputs introduced into the system design tool for the HYCAT 48 test.

Parameter name	**Value**
Δt	0.025
t_{total}	10.10
D_{diaph}	2.6×10^{-3}
$t_{trans,reg}$	0.18
$D_{cat,ch}$	50×10^{-3}
$L_{cat,ch}$	80×10^{-3}
$D_{cat,p}$	9×10^{-4}
$\rho_{cat,p}$	1000
$\eta_{c,cat}$	0.98
D_{ch} (t = 0 s)	25×10^{-3}
L_{ch}	498.8×10^{-3}
N_{ch}	100
$P_{ch,init}$ (t = 0 s)	101325
$T_{e,init}$ (t = 0 s)	298
$\dot{m}_{ox,init}$ (t = 0 s)	0
$\eta_{c,ch}$	0.86
D_{th}	16×10^{-3}
Σ	4.3
$D_{tuy,0}$	36×10^{-3}
α_{con}	45
α_{div}	15
N_{con}	400
N_{div}	200

4.1.1 Results of the injection sub-system for the HYCAT 48 test

The computed variables from the elements of the engine located before the combustion chamber (mass flow regulator and catalyst) that are involved in the simulation of the full HRE are: the oxidizer mass flow rate ($\dot{m}_{ox}$), the

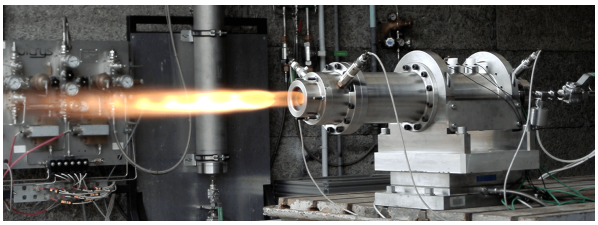

Figure 7: Firing of the HYCAT 48 test.

pressure at the entrance of the catalyst (P_{inj}), and the temperature at the exit (T_{cat}). For the HYCAT 48 test, a limiter concerning the increase of the flow velocity inside the catalyst has been imposed in order to restrict the rapid rise in $\dot{m}_{ox}$ at the beginning of the test. Otherwise, a very important ΔP_{cat} would be obtained, which may produce negative (and nonphysical) numerical values of pressure. For the HYCAT 48 test, a maximal slope limiter of $d\bar{u}_{cat}/dt = 30$ m/s^2 allowing to still provide physical pressure values, has been selected.

Figure 8 represents the experimental temporal evolution of the pressure in the oxidizer tank (P_{tank}). This variable is an input of the system design tool and, for the present simulations, is read from the experimental *txt* file. In this figure, two curves are depicted: the blue one, which is associated to the raw experimental data, obtained at a frequency of 5 kHz, and, therefore, subject to the measurements' noise; and the orange one, which represents the experimental measure smoothed by using a moving mean technique over 200 points (implying the averaging of data every 0.04 s). This smoothing procedure has been performed for all the experimental measurements in order to determine their underlying trend. For this input variable to the numerical domain, we observe that the tank pressure does not vary greatly during the firing, experiencing only a diminution at the beginning of the test (corresponding to the duration of the monopropellant phase), followed by a slight increase until establishing itself to an approximately constant value in the steady regime of the hybrid phase.

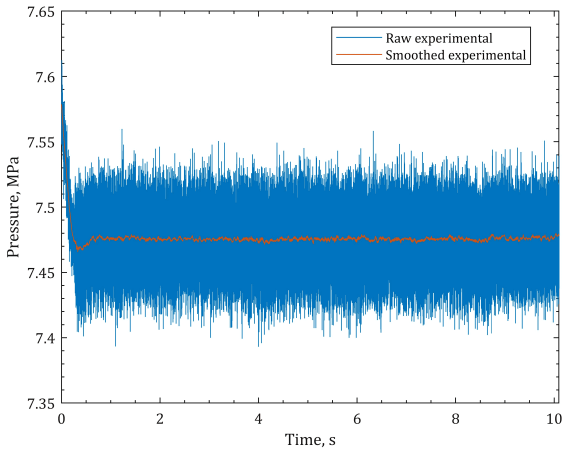

Figure 8: Temporal variation of the experimental pressure inside the tank for the HYCAT 48 test.

The hybrid phase in the test starts at 0.47 s. As regards the numerical simulation, two conditions are imposed to allow the start of the fuel pyrolysis phenomenon and the combustion process. The first requirement is that the surface temperature of the first node of the combustion chamber must be higher than the fusion temperature of the solid (see Table 2). The second one is that the temperature of the gaseous oxidizer at the entrance of the combustion chamber must be high enough to entail the reaction between the oxidizer and the pyrolyzed fuel gases. Our previous tests (12, 23 and 26) have shown that when using a catalyst, the temperature measured at the exit when the fuel pyrolysis starts is about 720 K, value that is also close to the auto-ignition temperature of ethylene (main substance produced by the pyrolysis of the HDPE fuel), which ranges from 720 to 760 K. These conditions lead to a hybrid phase starting at 0.7 s in the present computation, thus differing by 49% from the experiment (start at 0.47 s). Nonetheless, the duration difference between the simulation and the experiment is of only 2.38% if we only consider the hybrid phase duration

(t_{hyb}).

Figure 9 depicts the experimental (blue and orange curves) and numerical (black curve) variations through time of the pressure at the entrance of the catalyst (after passing the diaphragm element). A rapid increase of P_{inj} during the beginning of the monopropellant phase is obtained in both experimental and numerical evolutions. After this first transient phase, the pressure remains relatively constant during a short period of time, increasing quickly when the hybrid phase starts and diminishing slightly afterwards. Although these effects are correctly simulated by the computation, the pressure values provided are overestimated during the hybrid phase by 5.98%.

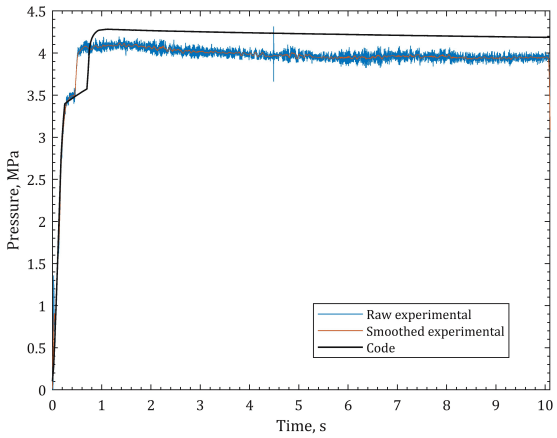

Figure 9: Temporal variation of pressure at the entrance of the catalyst in the experiment and the simulation for the HYCAT 48 test.

The temporal evolutions of the oxidizer mass flow rate retrieved experimentally and numerically are illustrated in Fig. 10. At the start of the test, the experimental value increases very quickly, reaching a maximum after which, it promptly decreases, remaining approximately constant for a short period of time. Then, during the start of the hybrid phase (at around 0.6 s), the faster increase in P_{inj} compared to the change in P_{tank} generates a slight decrease in the mass flow rate as described by Eq. (5). Later, $\dot{m}_{ox}$ grows a little during the hybrid phase because P_{inj} diminishes slightly (Fig. 9) while P_{tank} remains approximately constant (Fig. 8). When looking at the numerical variation, we observe that the linear increase applied to $\dot{m}_{ox}$ during the transient monopropellant phase (defined as $t_{trans,reg}$ = 0.18 s for this simulation) correctly reproduces the experimental evolution. Moreover, the little decrease of $\dot{m}_{ox}$ associated with the transition from the monopropellant to the hybrid phase is properly simulated by the code. As in the experiment, a peak in the mass flow rate evolution at the start of the firing (during the increase of $\dot{m}_{ox}$) is also observed in the numerical result, but without attaining the experimental value (at around 480 g/s). Hence, the main temporal effects are well captured by the simulation. Notwithstanding, contrary to what happened with the P_{inj} variable, the mass flow rate values are slightly underestimated throughout the test [see Eq. (5)], producing averaged relative differences of 2.63% in the hybrid phase with respect to the experiment.

Figure 11 depicts the experimental and numerical variation over time of the flow decomposition temperature at the exit of the catalyst. The experimental curve is obtained by averaging the measurements of the three temperature sensors employed in the test whose values differ less than 20% from the calculated mean. This way, we observe a non-monotonic increase of T_{cat} (peak at 0.4 s) due to the differences in the measurements regarding one of the sensors (see explanation in Sec. 3.2). In this graph, a slower rise of temperature is observed during the transient regime of the monopropellant phase when compared to the variations of P_{inj} and $\dot{m}_{ox}$ (Figs. 9 and 10, respectively). When the ignition of the engine happens, T_{cat} starts to increase a bit faster and, after the transient regime of the hybrid phase, reaches an approximately constant value. In comparison to the experiment, the simple 0-D model developed to simulate the complex catalyst system (linear temperature-increase model [Eq. (6)]) properly reproduces the rise of T_{cat} during the transient monopropellant phase, and only the experimental transient regime of the hybrid phase is not precisely simulated. Finally, in the steady regime of the hybrid phase, the program supplies a temperature value that is very close to the experimental one, differing only by 2.75% on average.

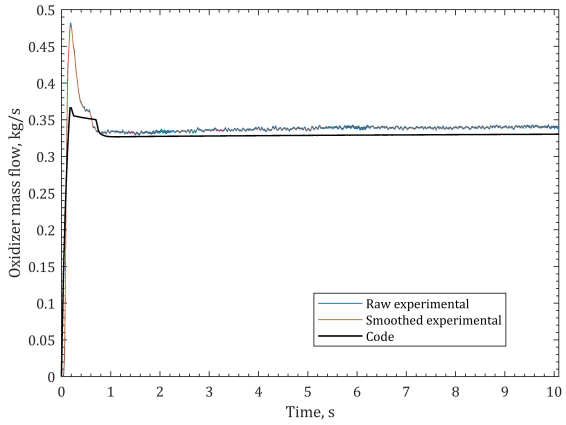

Figure 10: Temporal variation of the oxidizer mass flow in the experiment and the simulation for the HYCAT 48 test.

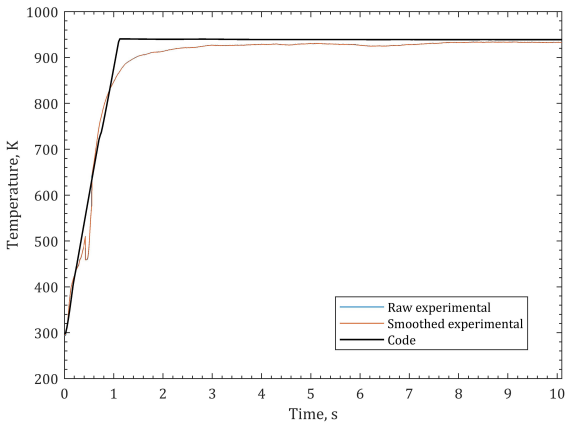

Figure 11: Temporal variation of the temperature at the exit of the catalyst in the experiment and the simulation for the HYCAT 48 test.

4.1.2 Results of the combustion chamber and nozzle elements for the HYCAT 48 test

In this subsection, the main variables related to the flow in the combustion chamber and the nozzle are analyzed and compared to the experiment (test 48).

Figure 12 depicts the temporal variation of the space-averaged combustion chamber pressure ($\bar{P}_{ch}$). As with the P_{inj} and T_{cat} variables, $\bar{P}_{ch}$ increases rapidly during the transitory regime of the monopropellant phase, attaining an approximately constant value (at around 1.20 MPa) once this transient has finished. However, the duration of this phenomenon is short for this test due to the high oxidizer mass flow (337 g/s) [see Eq. (7)]. Afterwards, when the energy of the flow transmitted to the solid fuel in the combustion chamber is high enough, the ignition of the engine happens, and the combustion process is initiated, producing an abrupt rise of the pressure inside the chamber. Opposite to the tendency of P_{inj} with time, the experimental $\bar{P}_{ch}$ value continues to grow slightly throughout the hybrid phase. This is because at the start of the test, the engine is cold, and the combustion is less efficient (low $\eta_{c,ch}$) since more energy is lost through the walls. Then, as time passes, less energy is employed to heat the chamber and the combustion becomes more efficient (higher $\eta_{c,ch}$), contributing to increase the pressure inside. Should erosion in the nozzle happen, it would however imply the diminution of pressure. Concerning the computation, although the ignition of the engine occurs later than in the real case, the monopropellant phase, as well as the rapid increase of $\bar{P}_{ch}$ at the beginning of the hybrid phase, are correctly simulated by the program. Nevertheless, contrary to what happens in the experiment, the pressure computed by the tool decreases during the hybrid phase. This is because no energy

loss nor nozzle erosion effects have been considered in our model, and the pressure in the chamber is only influenced by the mass flow rate imposed by the choked flow in the nozzle. Indeed, because the numerical fuel regression rate decreases over time while $\dot{m}_{ox}$ remains approximately constant (see Fig. 13), the injected mass of fuel gets reduced too, and so it happens with the total mass flow injected in the nozzle. As a consequence, pressure diminishes with time. Notwithstanding, on average, both the numerical and experimental $\bar{P}_{ch}$ values are very similar, differing only by 2.38%.

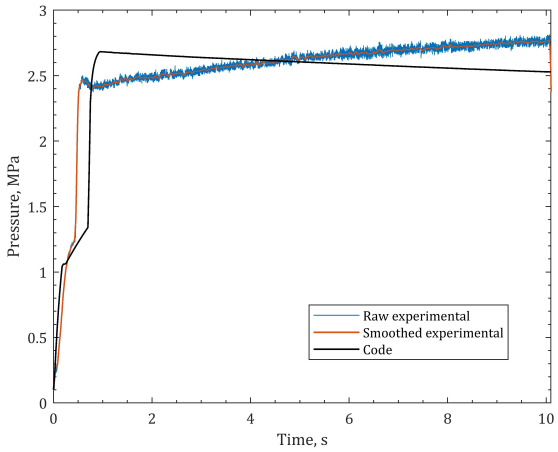

Figure 12: Temporal variation of the space-averaged pressure in the combustion chamber in the experiment and the simulation for the HYCAT 48 test.

Figure 13 illustrates the temporal evolution of the space-averaged fuel regression rate for this test. The experimental values remain practically constant all over the burning, whereas the numerical ones diminish throughout the test. The reduction of v_r obtained in the computation is related to the diminution of G_{ox}, this latter happening due to the increase of the cross-section of the channel whilst $\dot{m}_{ox}$ remains approximately constant. In the computation, the reduction of G_{ox} implies a diminution of the axial velocity of the flow and a thicker BL. The resulting further location of the flame from the wall reduces the heat transfers with the fuel surface, diminishing its temperature and, eventually, the pyrolysis rate through Eq. (13). Additionally, the relation between G_{ox} and v_r has been studied before in literature [29, 30, 31], where the theoretical analyses and semi-empirical laws have come to the expression $v_r = aG_{ox}^n$ $(a, n > 0)$, implying thus, an increase of v_r with G_{ox}, as it has been retrieved numerically.

On the contrary, in the experiment, the increase of chamber pressure with time and the constant $\eta_{c,ch}$ value assumed in the ballistic reconstruction technique to calculate the regression rate, may have slowed down the decrease of $\bar{v}_r$ that should have been obtained theoretically, producing as a result, a roughly constant regression rate. Indeed, several literature studies have found a positive dependency ratio between the pressure and the regression rate [32, 33]. Moreover, $\eta_{c,ch}$ is known to be smaller at the ignition of the engine (higher heat losses producing a less efficient combustion) and to grow afterwards. The increase of $\bar{P}_{ch}$ and $\eta_{c,ch}$ with time may have counterbalanced the effect of the diminution of G_{ox} on the regression rate, resulting in an approximately constant evolution of this latter. In the other HYCAT tests, whilst the experimental $\bar{v}_r$ values remain approximately constant, the developed model tends to generally overestimate the regression rates at the beginning of the firing and underestimate their values at the end. However, despite the discrepancy regarding the temporal variation of $\bar{v}_r$, the averaged relative difference between the numerical prediction and the test is only of 7.51%, remaining thus, below the maximum error of 30% specified for the validation of the system design tool.

Concerning the O/F mass ratio (computed as $\dot{m}_{ox}/\dot{m}_f$), the numerical and the experimental variations are contrary to each other (Fig. 14). In the experiment, $\dot{m}_f$ (obtained by the ballistic reconstruction technique) increases with time due to the larger burnt surface of fuel for a nearly constant v_r value, producing, by consequence, the diminution of mixing ratio. In the computation, however, the large reduction of $\bar{v}_r$ with time overpasses the burnt surface effect, contributing to diminish the computed $\dot{m}_f$ variable and increasing thus, the mixing ratio throughout the simulation. Nonetheless, in average, the relative difference between the experiment and the value provided by the tool is not very significant (4.35% only).

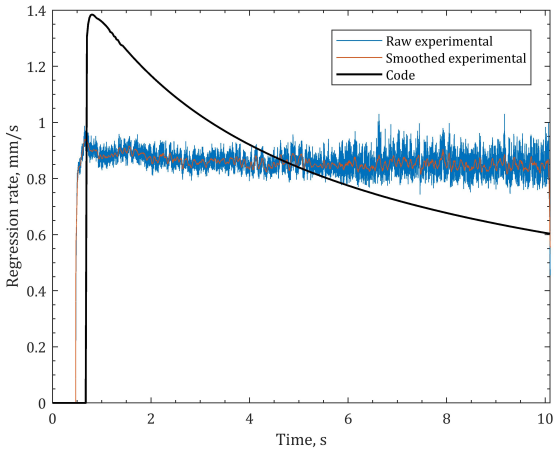

Figure 13: Temporal variation of the space-averaged fuel regression rate in the experiment and the simulation for the HYCAT 48 test.

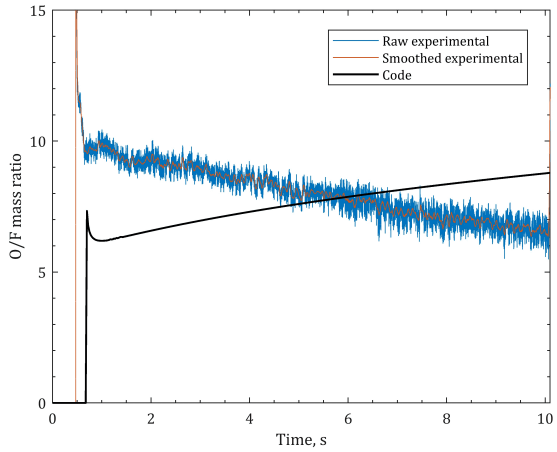

Figure 14: Temporal variation of the mixing ratio (post-chamber) in the experiment and the simulation for the HYCAT 48 test.

Figure 15 depicts a comparison between the local diameter of the fuel block computed by the tool at different times of the simulation and the final diameter obtained by the experimental measurements performed with the communicating vessel technique (Sec. 2.2). All the values have been normalized with the initial port diameter. The main difference between the simulation and the experiment resides in the spatial distribution along the channel. Indeed, the local diameter calculated by the program shows a decrease of the regression rate along the axis up to a minimum value, after which the fuel consumption increases progressively until the end of the chamber. This shape becomes more pronounced with time, being similar to the shapes retrieved in other experimental and numerical studies from literature [34, 35, 36]. Notwithstanding, the experimental local diameter measured at the end of the burn shows a fuel consumption region of concave shape that is not obtained numerically (characterized by a convex shape). Moreover, in the second part of the channel, the experimental diameter shows a decreasing regression rate tendency that is opposite to the one retrieved by the computation. The region of largest fuel consumption retrieved in the experiment may be produced by the presence of a recirculation zone generated by a jet impingement during the oxidizer injection. Indeed, the injector ring used for the axial injection of gaseous oxidizer is of the same diameter than the initial internal diameter of the fuel grain. Therefore, as the fuel is consumed and the port size increases, an impingement point due to the deviation of the flow entering into the channel appears and moves further from the entrance over the duration of the test. This physical mechanism allows the local enhancement of the fuel consumption. Despite

the differences concerning the spatial distribution of the diameter grain for this case, we have observed that, for the rest of the performed tests, the local variation of the experimental diameter shows the same behavior (similar shape) to the numerical one explained above, which is characterized by a convex shape with the largest fuel consumption obtained at the entrance of the combustion chamber. Furthermore, in this case, the space-averaged final diameter obtained by the computation and the measurements is very similar (averaged relative differences of 2.42%).

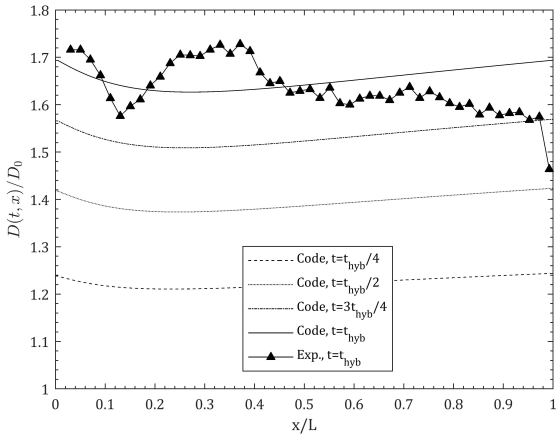

Figure 15: Local diameter of the fuel block at different times of the simulation compared with the experimental one at the end of the burn for the HYCAT 48 test.

Eventually, Figure 16 represents the thrust measurements of the engine provided by the dynamometric balance during the firing and the computed values by the code. Both the experimental and the numerical solutions follow a similar evolution to the one described by $\bar{P}_{ch}$ due to the positive dependence between this latter and the thrust [see Eq. (16)]. However, although the measured thrust increases from the start of the hybrid phase, it decreases slightly towards the end. This effect could have been due to the possible small wall erosion that may have happened in the nozzle, which is not modeled in the code. The graphite ablation could have affected the flow and the BL development inside the nozzle (not modeled neither), causing a small growth of the skin friction and the heat losses through the walls (not modeled neither), which would have entailed by consequence, a slight diminution of the engine performance. On the contrary, the numerical variation of this variable diminishes during the whole hybrid phase, as it happened with the numerical $\bar{P}_{ch}$ variable. Despite this, the averaged relative difference found between the computed and the experimental thrust values is very small, being below 1.70%.

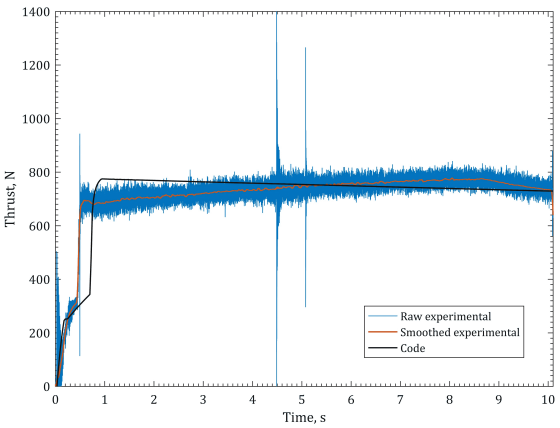

Figure 16: Temporal variation of the engine thrust in the experiment and the simulation for the HYCAT 48 test.

4.2 Summary of all the HYCAT tests results

The rest of the HYCAT tests have also been simulated with the system design tool. All of them have used as inputs the corresponding experimental P_{tank} measurements and the same thermodynamic properties defined in Table 2. The values of Table 3 associated to $\eta_{c,ch}$ and the geometric conditions of the grain and the nozzle have been adapted to each of the tests.

Generally, the temporal evolutions of the main computed variables for all the tests performed in the HYCAT engine are similar to the ones described in Secs. 4.1.1 and 4.1.2 for test 48, and mainly, the durations of the mono-propellant and the hybrid phases are modified on account of the effect that the oxidizer mass flow rate has on the catalyst.

Tables 4 and 5 show the time-averaged experimental values and uncertainties of the main variables during the hybrid phase for all the tests. These uncertainties come mainly from the errors of the sensors used to obtain the experimental measurements. In the case of D^{geo}_{final}, the uncertainties appearing in the tables correspond to the standard deviaton of the one-sided Student t-distribution with a 99% confidence level for the four diameter measurements performed for each grain with the communicating vessel measuring method. The duration of the hybrid phase (t_{hyb}) has been calculated by substracting the times at which this phase finishes and starts, each of them determined by the position of the largest peak of the quadratic time-derivative of the averaged chamber pressure. The corresponding uncertainties are computed by using the uncertainty propagation method to the errors related to the start and the end of the hybrid phase ($\delta t_{hyb,init}$ and $\delta t_{hyb,end}$, respectively): $\delta t_{hyb} = \sqrt{\delta t^2_{hyb,init} + \delta t^2_{hyb,end}}$ These latter ones are defined as the difference between the instants at which the aforementioned maximum peak is found and another one, situated downwards, characterized by a peak of value below 1% of the maximum one.

Table 6 supplies the relative differences and its uncertainties between the experimental measurements and the numerical values from the simulation. The numbers in red indicate the values that overpass the limit of accuracy established for the validation of our system design tool (30%). The relative difference (ε) of any numerical quantity (Φ_{num}) with respect to the corresponding experimental value (Φ_{exp}) has been calculated following the expression $\varepsilon = \frac{\Phi_{num}-\Phi_{exp}}{\Phi_{exp}} \times 100$. In these tables, no information concerning the thrust or the specific impulse of the engine appears for tests 23 and 46 since a problem encountered before the firing of these tests prevented us to make the thrust measurements.

In addition, two values of the regression rate variable are shown in the aforementioned tables: one of them has been acquired from the geometric measurements of the diameter through the communicating vessel technique ($\bar{v}^{geo}_r$) and the other is based on the conservation of volume of the grain at the end of the test ($\bar{v}^{vc}_r$). A larger value of $\bar{v}^{vc}_r$ over $\bar{v}^{geo}_r$ is retrieved, which is due to the fact that in the computation of $\bar{v}^{vc}_r$ the regression of the lateral faces is also taken into the calculation through Δm_f, whereas $\bar{v}^{geo}_r$ is deduced from the measurements of the internal block's diameter only. Moreover, the errors with respect to $\bar{v}^{geo}_r$ by using the measurements from the communicating vessel technique (reproducibility, parallax, capillarity) are generally larger than the errors induced by Δm_f in the estimation of $\bar{v}^{vc}_r$. It is also noticed that the greatest differences between $\bar{v}^{vc}_r$ and $\bar{v}^{geo}_r$ are generated for the tests 12 (17.67%), 23 (9.66%) and 26 (8.96%), where a larger space between the block and the injector ring was left. However, the influence of any of the two approaches in the estimation of v_r is less significant for the other tests (differences between 0.61% and 5.47%).

In general, for all the tests, the largest relative differences between the experiment and the computation come from the $\bar{v}^{geo}_r$, $\bar{v}^{vc}_r$, Δm_f and ϕ variables.

The HYCAT 12 and 23 tests are characterized by fuel grains of roughly the same size and a similar oxidizer mass flow rate (around 100 g/s). However, a larger regression rate is obtained in test 12 (about 12.3% bigger) than in test 23, which is related to the larger averaged G_{ox} (14.9% more significant). This effect is also retrieved in the numerical simulations. However, a more important discrepancy in $\bar{v}^{geo}_r$ between the experimental and the numerical values is found for test 12 (43.89% difference versus 24.52% in test 23). The precision provided by the computation of $\bar{v}^{geo}_r$ in test 12 is, indeed, below the specified limit for the system design tool. The better agreement between the numerical and the experimental values of this variable in test 23 -described by a flow of similar $\dot{m}_{ox}$ and slighlty smaller G_{ox}- could be due to the longer duration of the test. Indeed, in our 1.5-D model, it has already been observed the high dependence of the computed value of v_r with G_{ox}, implying the decrease of v_r with time due to the diminution of G_{ox} (see Sec. 4.1.2). This will eventually contribute to reduce the averaged regression rate and hence, produce a smaller difference with the experimental value. However, with the exception of the calculation of $\bar{v}^{geo}_r$ in test 12, the rest

Table 4: Time-averaged experimental results of HYCAT 12, 23, 26 and 46 tests.

Test	**HYCAT 12**	**HYCAT 23**	**HYCAT 26**	**HYCAT 46**
P_{inj}, MPa	$3.81 \pm 7 \times 10^{-3}$	$1.71 \pm 3 \times 10^{-3}$	$3.05 \pm 6 \times 10^{-3}$	$4.21 \pm 8 \times 10^{-3}$
T_{cat}, K	846.1 ± 29	868.5 ± 19	905.5 ± 17	870.8 ± 27
$\dot{m}_{ox}$, g/s	97.7 ± 0.2	105.1 ± 0.2	204.4 ± 0.4	302.6 ± 0.6
G_{ox}, kg/m^2/s	169.8 ± 2.5	144.6 ± 2.4	278.6 ± 7.4	374.8 ± 15.9
t_{hyb}, s	6.3 ± 0.31	17.28 ± 1.65	9.09 ± 0.51	9.40 ± 0.11
$\bar{P}_{ch}$, MPa	$3.6 \pm 5 \times 10^{-3}$	$1.21 \pm 5 \times 10^{-3}$	$2.24 \pm 4 \times 10^{-3}$	$2.08 \pm 4 \times 10^{-3}$
$\bar{D}^{geo}_{ch,final}$, mm	29.12 ± 0.3	35.86 ± 0.4	36.12 ± 0.7	39.13 ± 1.1
$\bar{D}^{vc}_{ch,final}$, mm	30.01 ± 0.07	37.02 ± 0.07	37.22 ± 0.07	39.21 ± 0.07
$\bar{v}^{geo}_r$, mm/s	0.327 ± 0.04	0.314 ± 0.04	0.612 ± 0.07	0.752 ± 0.07
$\bar{v}^{vc}_r$, mm/s	0.397 ± 0.03	0.348 ± 0.04	0.672 ± 0.04	0.756 ± 0.01
Δm_f, g	50 ± 0.2	135 ± 0.2	135.1 ± 0.2	172.7 ± 0.2
ϕ	12.31 ± 0.7	13.45 ± 1.3	13.75 ± 0.8	16.46 ± 0.2
$\eta_{c,ch}$	0.88 ± 0.03	0.88 ± 0.04	0.85 ± 0.02	0.94 ± 0.01
F, N	197.7 ± 0.4	-	394.2 ± 0.8	-
I_{sp}, s	190.8 ± 1.5	-	183.3 ± 1.4	-

Table 5: Time-averaged experimental results of HYCAT 47, 48 and 49 tests.

Test	**HYCAT 47**	**HYCAT 48**	**HYCAT 49**
P_{inj}, MPa	$3.80 \pm 8 \times 10^{-3}$	$3.98 \pm 8 \times 10^{-3}$	$3.77 \pm 8 \times 10^{-3}$
T_{cat}, K	913.0 ± 6	909.1 ± 17	907.5 ± 32
$\dot{m}_{ox}$, g/s	328.5 ± 0.7	337.8 ± 0.7	348.3 ± 0.7
G_{ox}, kg/m^2/s	187.9 ± 0.9	395.0 ± 13.2	230.1 ± 5.0
t_{hyb}, s	9.28 ± 0.08	9.64 ± 0.06	9.68 ± 0.07
$\bar{P}_{ch}$, MPa	$1.99 \pm 4 \times 10^{-3}$	$2.66 \pm 5 \times 10^{-3}$	$2.41 \pm 5 \times 10^{-3}$
$\bar{D}^{geo}_{ch,final}$, mm	46.79 ± 1.3	41.0 ± 1	47.79 ± 0.8
$\bar{D}^{vc}_{ch,final}$, mm	47.18 ± 0.07	41.51 ± 0.06	48.10 ± 0.06
$\bar{v}^{geo}_r$, mm/s	0.366 ± 0.08	0.829 ± 0.06	0.403 ± 0.05
$\bar{v}^{vc}_r$, mm/s	0.387 ± 0.01	0.856 ± 0.01	0.419 ± 0.01
Δm_f, g	116.8 ± 0.2	408.9 ± 0.2	266.7 ± 0.2
ϕ	26.11 ± 0.3	7.97 ± 0.1	12.63 ± 0.1
$\eta_{c,ch}$	0.94 ± 0.01	0.86 ± 0.01	0.87 ± 0.01
F, N	542.6 ± 1.1	737.9 ± 1.5	675.0 ± 1.3
I_{sp}, s	162.2 ± 0.7	197.8 ± 0.9	183.1 ± 0.8

Table 6: Relative differences (in %) between the experiment and the simulation for the HYCAT 12, 23, 26, 46, 47, 48 and 49 tests.

Test	HYCAT 12	HYCAT 23	HYCAT 26	HYCAT 46	HYCAT 47	HYCAT 48	HYCAT 49
P_{inj}	2.31 ± 0.2	−5.28 ± 0.2	0.56 ± 0.2	−6.10 ± 0.2	2.15 ± 0.2	5.98 ± 0.2	9.94 ± 0.2
T_{cat}	3.48 ± 2.0	2.17 ± 1.0	1.83 ± 0.2	3.14 ± 3.1	1.87 ± 0.7	2.78 ± 2.0	3.63 ± 3.6
$\dot{m}_{ox}$	−1.12 ± 0.2	−2.31 ± 0.2	0.45 ± 0.2	7.12 ± 0.2	−0.32 ± 0.2	−2.63 ± 0.2	−5.30 ± 0.2
t_{hyb}	5.15 ± 3.9	9.41 ± 5.5	−3.44 ± 2.7	−1.12 ± 0.5	1.07 ± 0.8	−2.38 ± 0.6	−1.80 ± 0.8
$\bar{P}_{ch}$	4.70 ± 0.2	2.62 ± 0.4	0.54 ± 0.2	9.11 ± 0.2	7.44 ± 0.21	−2.38 ± 0.20	2.69 ± 0.2
$\bar{D}^{geo}_{ch,final}$	7.04 ± 1.1	8.15 ± 1.2	2.76 ± 2.0	4.37 ± 3.0	6.10 ± 3.0	2.42 ± 1.2	4.27 ± 1.8
$\bar{D}^{vc}_{ch,final}$	3.99 ± 0.1	4.84 ± 0.1	0.30 ± 0.2	4.05 ± 0.2	5.13 ± 0.2	0.15 ± 0.1	3.56 ± 0.1
$\bar{v}^{geo}_r$	43.89 ± 17.6	24.52 ± 16.7	13.38 ± 11.5	13.69 ± 10.6	45.46 ± 29.9	7.51 ± 5.8	29.96 ± 15.6
$\bar{v}^{vc}_r$	17.31 ± 8.6	11.92 ± 11.7	6.70 ± 0.5	12.06 ± 2.2	31.76 ± 3.3	1.98 ± 1.4	23.18 ± 2.7
Δm_f	25.57 ± 0.5	17.82 ± 0.2	0.78 ± 0.2	13.12 ± 0.1	38.96 ± 0.2	0.66 ± 0.1	24.51 ± 0.1
ϕ	−17.03 ± 4.6	−12.68 ± 8.7	−6.0 ± 0.3	−5.15 ± 1.4	−26.29 ± 1.6	−4.35 ± 0.9	−24.97 ± 0.8
F	9.28 ± 0.2	-	−5.81 ± 0.2	-	10.41 ± 0.2	1.70 ± 0.2	5.67 ± 0.2
I_{sp}	8.98 ± 0.9	-	−6.27 ± 0.7	-	9.57 ± 0.3	3.84 ± 0.5	8.99 ± 0.5

of the variables in both tests are pretty well estimated through the developed models, generating relative differences with the experiments that are below the required threshold of 30% for the system design tool. In fact, out of the four variables mentioned above ($\bar{v}^{geo}_r$, $\bar{v}^{vc}_r$, Δm_f and ϕ), the rest of them present relative differences below 10% with the tests, constituting, thus, a good approximation for the precision searched.

In the HYCAT 26 test, which operates at a higher oxidizer mass flow rate than tests 12 and 23, we are able to provide a better estimation of the $\bar{v}_r$ values. In agreement with literature, the increase of G_{ox} (1.6 times larger than in test 12) generates higher fuel regression rates in both the experiment and the simulation.

Test 46 is characterized by a larger $\dot{m}_{ox}$ than test 26 and a grain of identical initial port size. The retrieved regression rate for this new test is thus, larger too (more important G_{ox}). However, although v_r (and by consequence $\dot{m}_f$) increases with $\dot{m}_{ox}$ for a specific size of the fuel block, the increment produced in $\dot{m}_f$ is smaller than in $\dot{m}_{ox}$, generating an increase of the mixing ratio which moves away from its optimum value (next to stoichiometry). As a consequence, the combustion efficiency will decrease, restraining the increment of the regression rate in the experiment that would have been expected. Neverhteless, the effect of the O/F ratio has a lesser impact on the code. Indeed, the flame is considered to happen at stoichiometric conditions and ϕ intervenes specially in the nozzle flow by affecting the numerical value of pressure required in the combustion chamber. However, a previous sensitivity analysis of the 1.5-D combustion chamber model [37] has shown that, for example, the increase of the combustion chamber pressure value by 0.5 MPa, entails an increment of $\bar{v}_r$ by 1.12% only. Therefore, due to the simplifications taken in the modeling, the impact of the O/F mass ratio on the simulation is less significant in comparison to the experiment. Hence, the larger mixing ratio of HYCAT 46 test (ϕ = 16.46), together with the overestimation of the computed $\dot{m}_{ox}$ value that is made for this test, implies larger differences of $\bar{v}^{geo}_r$ and $\bar{v}^{vc}_r$ between the simulation and the test when comparing with the ones retrieved for test 26 (with the smaller ϕ = 13.75). Nevertheless, despite this, the time-averaged relative differences of the computed variables with the experimental values for both 26 and 46 tests are below 14%, remaining thus, within the defined accuracy limit for the tool.

Differently, the HYCAT 47 test, performed with a grain of larger port size and at similar oxidizer mass flow rate than test 46 ($\dot{m}_{ox} \approx$ 329 g/s), is, therefore, characterized by a smaller G_{ox} than the ones from tests 26 and 46, but, at the same time, higher than those retrieved in tests 12 and 23. Nonetheless, because the O/F mass ratio is very large (ϕ = 26.11, being the largest of all the performed tests), far from the stoichiometric value for this couple (ϕ_{st} = 8.33), and knowing that the impact produced by the diminution of G_{ox} on the reduction of v_r is much more significant in the experiment than in the simulation, the relative differences between the experimental and numerical values of $\bar{v}^{geo}_r$ and Δm_f increase in this case up to 45.46%. Concerning the rest of the variables, the differences fall below the threshold of 30%.

Increasing the fuel block length when maintaining the same port diameter of the grain and approximately the same flow characteristics at the inlet of the channel, contributes to increase the total mass burnt of fuel in the combustion chamber (larger burnt surface), diminishing ϕ and approaching it to the optimum value. This fact will contribute to

enlarge the overall regression rate in the channel due to the improvement of the combustion process. This is the case of HYCAT 48 and 49 tests, which, despite having a slightly larger G_{ox} than their respective tests using shorter grains (46 and 47), the retrieved experimental $\bar{v}_r$ is, in part, increased due to the larger mixing ratio. As we have seen in Secs. 4.1.1 and 4.1.2 for test 48, the relative differences of the computed variables with the experiment remain below 8%, with the estimation of $\bar{v}_r$ being very close to the experimental one. The variables of the HYCAT 49 test are better estimated than in test 47 as well, due to the proximity of ϕ to the stoichiometric value. The largest relative differences are below the limit established for the validation of the system design tool. These are produced for both $\bar{v}_r^{geo}$ and $\bar{v}_r^{vc}$ (29.96 and 23.18% respectively), Δm_f (24.51%) and $\dot{m}_{ox}/\dot{m}_f$ (24.97%). Concerning the rest of the variables, the differences are below 10%.

Figure 17 illustrates the dependence of the time and space averaged regression rate values with the oxidizer mass flux from the experiment (blue markers) -obtained through the communicating vessel technique-, and the simulation (black markers), which implies an increase in fuel consumption with G_{ox}. The graph also represents a polynomial trend curve that fits the best the experimental results, and a power law matching the numerical values ($\mathcal{R}^2 = 0.97$). This latter results to be in agreement with several literature data for this O/F couple [38, 39], producing absolute relative differences with the references up to 34%. The experimental curve seems to present a lesser dependence of v_r with G_{ox} for the smallest values ($G_{ox} < 200$ kg/m^2/s). This effect could be due to the more important radiative heat fluxes that are produced at lower G_{ox} [34] and contribute to increase the regression rate with respect to the case where these heat fluxes were not considered (as it is the case for our 1.5-D combustion chamber model).

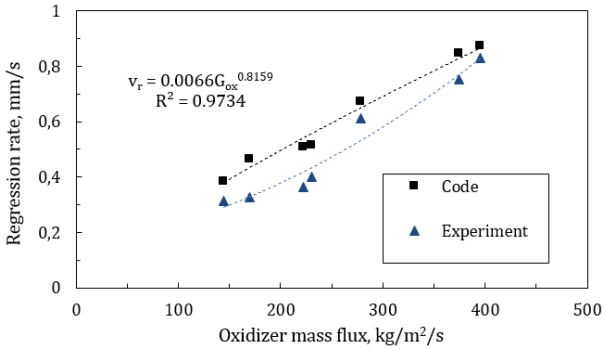

Figure 17: Dependence of the experimental and numerical space-time averaged regression rate with the oxidizer mass flux for all the HYCAT tests.

To sum up, the relative differences concerning the fuel regression rate happen to be especially large for the requirements of the system design tool (errors below 30%) in two of the realized tests (12 and 47). On one hand, the HYCAT 12 test is characterized by experiencing one of the lowest G_{ox} from all the performed tests (< 200 kg/m^2/s) and by being the shortest firing ($t_{hyb} = 6.3$ s), which, as we have seen in Sec. 4.1.2, affects the averaged v_r value since this one decreases with time in the numerical simulation. On the other hand, test 47 has not a particularly high G_{ox} neither (222 kg/m^2/s), and the retrieved mixing ratio is the largest from all the completed tests ($\phi = 26.11$), being far from the hypothesis of stoichiometric combustion ($\phi_{st} = 8.31$) taken for the flame model in the chamber. On the contrary, in HYCAT 49 test, although characterized by a similar G_{ox} than test 47, because ϕ is lower and closer to the stoichiometric conditions, a better estimation of $\bar{v}_r$ is provided by the numerical simulation. Moreover, the better agreement of the computed $\bar{v}_r$ with the experimental value of test 23 in spite of the low G_{ox} (similar to that of test 12) is due mostly to the longer duration of the firing, which contributes to reduce the averaged v_r value of the simulation. Eventually, the rest of the tests (26, 46, 48 and 49), performed at higher G_{ox} and at moderate mixing ratios ($\phi < 17$) provide better estimations of the regression rate and the consumed mass of fuel that satisfy the accuracy requirements for the validation of the system design tool.

5. Conclusions

A system design tool able to simulate a full HRE propulsion system in fast computation times from a desktop computer has been developed in this paper with the purpose of using it during the first pre-design phases of the engine. This application gathers several simple models of the main elements consituting an engine of axial catalytic

injection: 0-D models for the mass flow regulator and the catalyst components; a 1.5-D combustion chamber model; and a 1-D nozzle model. These last two have already been developed and validated in previous work. The algorithm implemented in this newly developed tool to solve the whole system of equations consists of a convergence technique established between the three main aforementioned parts of the engine, and has been developed in such a way that allows the simulation of one or more elements composing the engine. Seven experiments performed on the laboratory's HRE (HYCAT) by using an axial catalytic injection of hydrogen peroxide as the oxidizer and HDPE as the fuel have been employed to validate the system design tool. The retrieved results show, for all the tests, an especially good agreement in the estimation of the mass flow rate and the pressure values, as well as the thrust and the specific impulse of the engine (time-averaged relative differences with the measurements below 11%).

The main physical effects are pretty well simulated by the program (monopropellant and hybrid phases). Notwithstanding, some temporal trends retrieved from the computation are not exactly the same as in the experiment due to the lack of modeling of certain physics. Such is the case of the combustion chamber pressure, where the heat losses through the walls or the change of $\eta_{c,ch}$ in time are not modeled.

The relative differences between the experiment and the code for the v_r variable -main parameter characterizing the performances in a HRE- become more important when using the values obtained through the geometric measurement of the diameter at the end of the burn than when employing the volume conservation principle (total consumed mass of fuel) to calculate the diameter. This is mainly due to the larger uncertainties associated to the geometric measurements and the possible overestimation of the port diameter when using the burnt mass of fuel because of the regression of the lateral faces.

Moreover, increasing the length of the fuel block leads to the increase of the total consumed mass of fuel and yields, for a given $\dot{m}_{ox}$, a decrease of the O/F mass ratio, approaching its value to the optimum (stoichiometric one) and producing, by consequence, a general rise in $\bar{v}_r$ that is related to a better combustion. Hence, the relative differences of $\bar{v}_r$ between the numerical simulation and the experiment will decrease since ϕ will be closer to the stoichiometric value that has been employed to describe the flame and the combustion in the 1.5-D chamber model.

The comparison between the time-averaged values from the simulations and the tests shows that the greatest relative differences with the experiment happen with the fuel regression rate, the total consumed mass of fuel, and the mixing ratio variables. The averaged values of the computed regression rate are overestimated in all of the seven tests (about 25.5% on average), and so it happens with the consumed mass of fuel (17.3%), producing as a consequence, an underestimation of the mixing ratio (averaged differences of 13.8%) for an oxidizer mass flow that is generally well estimated (errors of 2.8%). The relative differences concerning the fuel regression rate turn out to be satisfactory for the desired application tool in five of the seven tests analyzed (tests 23, 26, 46, 48 and 49), hence, presenting errors below 30%. This good agreement has been obtained in firings with a duration of 10 s or more, characterized by high G_{ox} flows (> 230 kg/m^2/s) and by a mixing ratio that is not very far from stoichiometry (equivalence ratio ϕ/ϕ_{st} bigger than 0.65).

In conclusion, the developed system design tool succeeds in simulating the main physical phenomena present in a HRE and provides a good averaged accuracy of the main variables characterizing the flow in this engine for predesign engine applications (errors below 30%). Therefore, the tool can be considered to be experimentally validated in a specific operation range of the engine, offering satisfying results in the simulation of a hybrid space propulsion system.

Aknowledgements

Special thanks to ONERA and CNES for financially supporting this research and the Propulsion Laboratory Research Unit of ONERA for the realization of the experimental campaign on the HYCAT test bench.

Appendix A (Transient 1-D nozzle equations)

The 1-D transient Euler equations of continuity [Eq. (18)], momentum [Eq. (19)] and energy [Eq. (20)] describing the flow inside the nozzle of the engine are presented in this appendix in terms of the non-dimensional variables: $\rho' = \frac{\rho}{\rho_{ch,N+1}}$; $T' = \frac{T}{T_{ch,N+1}}$; $A' = \frac{A}{A_{th}}$; $t' = \frac{t}{L/a_{ch,N+1}}$; $P' = \frac{P}{P_{ch,N+1}}$; $u' = \frac{u}{a_{ch,N+1}}$ and $x' = \frac{x}{L_{nozzle}}$.

$$\frac{\partial}{\partial t'}(\rho' A') + \frac{\partial}{\partial x'}(\rho' A' u') = 0 \tag{18}$$

$$\frac{\partial}{\partial t'}(\rho' A' u') + \frac{\partial}{\partial x'}\left(\rho' A' u'^2 + \frac{1}{\gamma}\rho' A'\right) = \frac{1}{\gamma} p' \frac{\partial A'}{\partial x'} \tag{19}$$

$$\frac{\partial}{\partial t'}\left[\rho'\left(\frac{T'}{\gamma - 1} + \frac{\gamma}{2}u'^2\right)A'\right] + \frac{\partial}{\partial x'}\left[\rho'\left(\frac{T'}{\gamma - 1} + \frac{\gamma}{2}u'^2\right)A' u' + + P' A' u'\right] = 0 \tag{20}$$

References

[1] D. Bianchi, G. Leccese, F. Nasuti, M. Onofri, and C. Carmicino. Modeling of high density polyethylene regression rate in the simulation of hybrid rocket flowfields. *Aerospace*, 6(88), 2019.

[2] A. Coronetti and S. William. Numerical analysis of hybrid rocket combustion. *Journal of Propulsion and Power*, 29:371–384, 03 2013.

[3] G. Di Martino, C. Carmicino, and R. Savino. Transient computational thermofluid-dynamic simulation of hybrid rocket internal ballistics. *Journal of Propulsion and Power*, 33:1395–1409, 03 2017.

[4] T.V. Chelaru and F. Mingireanu. Hybrid rocket engine, theoretical model and experiment. *Acta Astronautica*, 68(11):1891–1902, June 2011.

[5] B. Genevieve, J. Pitot, and M. Brooks. A computational tool for predicting hybrid rocket motor performance. *R&D Journal*, 33:56–65, 08 2017.

[6] P.M. Zolla, M.T. Migliorino, D. Bianchi, F. Nasuti, R.C. Pellegrini, and E. Cavallini. A computational tool for the design of hybrid rockets. *Aerotecnica Missili & Spazio*, 100(4):387–397, 2021.

[7] M. Gieras and A. Gorgeri. Numerical modelling of the hybrid rocket engine performance. *Propulsion and Power Research*, 10(1):15–22, 2021.

[8] Empresarios Agrupados. *European Space Propulsion System Simulation (ESPSS)*. Nov. 2013.

[9] F.S. Mechentel. *Preliminary Design of a Hybrid Motor for Small-Satellite Propulsion*. PhD thesis, Dept. of Aeronautics and Astronautics, Stanford University, Stanford, CA, 2019.

[10] L. Casalino and D. Pastrone. Oxidizer control and optimal design of hybrid rockets for small satellites. *Journal of Propulsion and Power*, 21(2):230–238, 2005.

[11] E. Toson and A.M. Karabeyoglu. Design and optimization of hybrid propulsion systems for in-space application. In *51st AIAA/SAE/ASEE Joint Propulsion Conference*, Orlando, FL, July 2015. AIAA Paper 2015-3937.

[12] C. Bayeux, E. Radenac, and P. Villedieu. Theory and validation of a 2D finite-volume integral boundary-layer method for icing applications. *AIAA Journal*, 57(3):1092–1112, March 2019.

[13] J. Y. Lestrade. *Modeling of the Regression of Liquefiable Fuels in a Hybrid Rocket – Modélisation de la Régression des Combustibles Liquéfiables dans un Moteur Hybride*. PhD thesis, Institut Supérieur de l'Aéronautique et de l'Espace (ISAE), 2012.

[14] J. Y. Lestrade, J. Anthoine, O. Verberne, A. Boiron, G. Khimeche, and C. Figus. Experimental demonstration of the vacuum specific impulse of a hybrid rocket engine. *Journal of Spacecraft and Rockets*, 54, 10 2016.

[15] J. Messineo, K. Kitagawa, C. Carmicino, T. Shimada, and C. Paravan. Reconstructed ballistic data versus wax regression-rate intrusive measurement in a hybrid rocket. *Journal of Spacecraft and Rockets*, 57(6):1295–1308, 2020.

[16] Christopher Glaser, Riccardo Gelain, Artur Bertoldi, Jouke Hijlkema, P. Hendrick, and Jerome Anthoine. Experimental investigation of stepped fuel grain geometries in hybrid rocket engines. In *9th European Conference for Aeronautics and Space Sciences (EUCASS)*, Lille, France, June 2022.

[17] J. E. Durand, J. Y. Lestrade, and J. Anthoine. Restitution methodology for space and time dependent solid-fuel port diameter evolution in hybrid rocket engines. *Aerospace Science and Technology*, 110:1–15, Jan. 2021.

[18] S. A. Whitmore and S. N. Chandler. Engineering model for self-pressurizing saturated-N2O-propellant feed systems. *Journal of Propulsion and Power*, 6(4), July 2010.

[19] A. Pasini, L. Torre, L. Romeo, A. Cervone, and L. d'Agostino. Reduced-order model for H2O2 catalytic reactor performance analysis. *Journal of Propulsion and Power*, 26(3):446–453, 2010.

[20] S. A. Whitmore, C. J. Martinez, and D. P Merkley. Catalyst development for an arc-ignited hydrogen peroxide/ABS hybrid rocket system. *Aeronautics and Aerospace Open Access Journal*, 2(6):356–388, Nov. 2018.

[21] M. Maestri and A. Cuoci. Coupling cfd with detailed microkinetic modeling in heterogeneous catalysis. *Chemical Engineering Science*, 96(12):106–117, 2013.

[22] S. Gordon and B. J. McBride. Computer program for calculation of complex chemical equilibrium compositions and applications. *NASA reference publication 1311*, Oct. 1994.
[23] J. Y. Lestrade, P. Prévot, J. Messineo, J. Anthoine, S. Casu, and B. Geiger. Development of a catalyst for highly concentrated hydrogen peroxide. In *Space Propulsion 2016*, Rome, Italy, June 2016.
[24] S. Ergun. Fluid flow through packed columns. *Journal of Chemical Engineering Progress*, 48(2):89–94, 1952.
[25] O. Bey and G. Eigenberger. Fluid flow through catalyst filled tubes. *Chemical Engineering Science*, 52(8):1365–1376, 1997.
[26] E. Quero Granado, J. Hijlkema, J.Y. Lestrade, and J. Anthoine. Pseudo-2-dimensional modeling and validation of a hybrid rocket combustion chamber. *Journal of Propulsion and Power*, pages 1–16, June 2022.
[27] N. Gascoin, P. Gillard, A. Mangeot, and A. Navarro-Rodriguez. Literature survey for a first choice of a fuel-oxidiser couple for hybrid propulsion based on kinetic justifications. *Journal of Analytical and Applied Pyrolysis*, 94:1–9, March 2012.
[28] G. Lengellé, B. Fourest, J. Godon, and C. Guin. Condensed-phase behavior and ablation rate of fuels for hybrid propulsion. In *29th Joint Propulsion Conference and Exhibit*. AIAA Paper 93-2413, June 1993.
[29] G. A. Marxman and M. Gilbert. Turbulent boundary layer combustion in the hybrid rocket. *Symposium (International) on Combustion*, 9(1):371–383, 1963.
[30] C. Carmicino and A. Sorge. Role of injection in hybrid rockets regression rate behaviour. *Journal of Propulsion and Power*, 21(4):606–612, 2005.
[31] M. Chiaverini, G. Harting, K. K. Kuo, and A. Peretz. Regression rate and heat transfer correlations for hybrid rocket combustion. *Journal of Propulsion and Power*, 17(1):99–110, 2001.
[32] D. Helman, M. Wolfshtein, and Y. Manheimer-Timnat. Theoretical investigation of hybrid rocket combustion by numerical methods. *Journal of Combustion and Flame*, 22(2):171–190, 1974.
[33] L. D. Smoot and C. F. Price. Pressure dependence of hybrid fuel regression rates. *AIAA Journal*, 5(1):102–106, 1967.
[34] M. Chiaverini, D. Johnson, K. K. Kuo, Y. C. Lu, G. Risha, and N. Serin. Regression rate behavior of hybrid rocket solid fuels. *Journal of Propulsion and Power*, 16(1):125–132, Jan. 2000.
[35] G. Gariani, F. Maggi, and L. Galfetti. Numerical simulation of HTPB combustion in a 2D hybrid slab combustor. *Acta Astronautica*, 69:289–296, Sept. 2011.
[36] P. George, S. Krishnan, L. Ramachandran, M. Ravindran, and M. Varkey. Fuel regression rate in hydroxyl-terminated-polybutadiene/gaseous-oxygen hybrid rocket motors. *Journal of Propulsion and Power*, 17(1):35–42, 2001.
[37] E. Quero Granado, J. Hijlkema, J.Y. Lestrade, and J. Antthoine. Parametric study of a 1.5-D combustion chamber model on the hybrid rocket engine performances. In *9th European Conference for Aeronautics and Aerospace Sciences (EUCASS)*, Lille, France, June 2022.
[38] E. Wernimont and S. Heister. Combustion experiments in hydrogen peroxide/polyethylene hybrid rocket with catalytic ignition. *Journal of Propulsion and Power*, 16:318–326, March 2000.
[39] B. Ahn, H. Kang, E. Lee, Y. Yun, and S. Kwon. Design of multiport grain with hydrogen peroxide hybrid rocket. *Journal of Propulsion and Power*, 34(5):1189–1197, 2018.